Kite as a Sensor: Wind and State Estimation in Tethered Flying Systems

Oriol Cayon[1], Simon Watson[1], and Roland Schmehl[1]

[1]Faculty of Aerospace Engineering, Delft University of Technology, 2629 HS Delft, the Netherlands

Correspondence: Oriol Cayon (o.cayon@tudelft.nl)

Abstract. Airborne wind energy systems (AWESs) leverage the generally less variable and higher wind speeds at increased altitudes by utilizing kites, with significantly reduced material costs compared to conventional wind turbines. Energy is commonly harnessed by flying crosswind trajectories, which allow the kite to achieve speeds significantly higher than the ambient wind speed. However, the airborne nature of these systems demands active control and makes them highly sensitive to changes in wind conditions, making accurate wind measurements essential for steering the kite along its optimal trajectory. This paper presents an advanced sensor fusion technique based on an iterated extended Kalman filter (EKF) for state and wind estimation for AWESs. By integrating position, velocity, tether force, and reeling speed, this method provides accurate estimations of system dynamics, including kite orientation and tether shape. The estimates of the wind speed and direction are compared to lidar measurements, showing a strong agreement across various atmospheric conditions. The results demonstrate that this approach can effectively capture the transient dynamics of atmospheric wind using sensors typically already present in AWESs, making it suitable for supervisory control strategies and ultimately enhancing energy efficiency and system reliability across diverse atmospheric conditions.

1 Introduction

Airborne wind energy systems (AWESs) harness wind energy with tethered aerial devices, substantially reducing material usage compared to conventional wind turbines by employing one or more tethers and a flying apparatus instead of towers and blades. This reduction has the potential to lower the costs associated with wind energy production but also allows for the exploitation of higher-altitude winds, which are generally less variable and of a higher average speed than those at ground level.

Despite these advantages, AWESs face significant challenges, particularly regarding system robustness against the complexities of atmospheric wind dynamics. The motion of the kite during crosswind flight is strongly influenced by the wind, which largely dictates the flight speed and the tether force. This dependency makes the system highly susceptible to changes in wind speed and direction. For soft kites, the low mass of the tensile structure allows for rapid adaptation to changes in wind speed, making this type of kite particularly sensitive to turbulence and gusts. Therefore, a detailed understanding of wind dynamics at the operational altitudes is crucial.

25   Above the well-studied surface layer, logarithmic wind profiles may not accurately represent the variation of wind speed with height, and phenomena such as wind veer and low-level jets become increasingly significant. As a result, it is crucial to adapt the kite's trajectory to these specific higher-altitude wind conditions, which necessitates reliable wind measurements. This need for accurate wind data can be met through remote sensing devices such as lidar (Sommerfeld et al., 2019), or by using the kite itself as a sensor.

30   Using the aerial device as a sensor eliminates the need for additional equipment beyond what is already used for kite control and allows wind velocity information to be integrated into a supervisory control strategy for the AWES. This integration enables the system to adjust the flight trajectory in response to changing wind conditions, optimizing performance and aiding in high-level decisions, whether to take-off or to land.

    A common method for determining ambient wind conditions at the kite involves mounting flow sensors on the kite to 35 measure the apparent wind speed and direction. Pitot tubes are frequently used, in varying configurations. Five-hole probes and single-hole probes combined with two flow vanes can measure the three-dimensional velocity vector of the apparent wind (Elfert et al., 2024; Borobia-Moreno et al., 2021; Oehler and Schmehl, 2019), allowing for the determination of ambient wind speed, provided the kite's velocity is known. Simpler setups with single-hole probes alone (Vlugt et al., 2013; Borobia et al., 2018) or with one vane (Schelbergen, 2024) are also used but do not capture the full three-dimensional velocity, limiting their 40 capability.

    However, this approach comes with significant challenges. The accuracy of the measurements depends heavily on the sensor's position, mounting method, and regular maintenance and recalibration. For soft kites, which undergo substantial deformation during flight along with vibrating bridle lines and fluttering membrane, the collected data can become excessively noisy and unreliable (Dunker, 2018; Leuthold, 2015). These challenges, particularly for tensile, lightweight kite systems, highlight 45 the need for more advanced approaches.

    One effective solution is sensor fusion, which combines data from multiple sensors integrated into the AWES to provide a more robust and consistent representation of the kite state and wind characteristics. Sensor fusion relies on a time-dependent model that represents the system's dynamics. By integrating sensor data within this model, the method enhances the reliability of the measured states and can also serve to estimate quantities such as wind speed and direction. Depending on the model's 50 complexity, the estimated state may encompass not only the kite's position and velocity but also its aerodynamic characteristics and the tether sag, resulting in a more comprehensive understanding of the system's dynamics.

    Numerous studies have investigated sensor fusion techniques for AWE state and wind estimation (Table 1). For instance, Fagiano et al. (2013, 2014) proposed an extended Kalman filter (EKF) to estimate the kinematics of a tethered aircraft, using a purely kinematic model and evaluating various sensor configurations, including satellite-based global positioning system 55 (GPS) and tether angle measurements. Similarly, Polzin et al. (2017); Wood et al. (2018) explored configurations incorporating inertial measurement units (IMUs), tether angles, and camera tracking, introducing a novel kinematic model that accounts for tether dynamics and sag through time delays and ground velocity differences. This study also addressed kite steering delays by modelling the yawing motion with a linear turn rate law. To further address tether sag, Freter et al. (2020) proposed an adaptive Kalman filter with variable weights based on tether force, combining data from load cells, tether angles, IMUs, and camera

Table 1. Summary of studies on sensor fusion for AWESs.

Study	Filter Type	Minimum Required Measurements	Kite Model	Tether Model
Fagiano et al. (2013, 2014)	EKF	Position, acceleration, orientation, orientation rates	Kinematic	Straight & Inelastic
Polzin et al. (2017); Wood et al. (2018)	EKF	Position, orientation, orientation rates	Kinematic	Straight & Inelastic
Freter et al. (2020)	Adaptive EKF	Position, acceleration, tether force	Kinematic	Straight & Inelastic
Williams et al. (2008)	Square-root UKF	Position, tether force and direction, tether length and reeling speed	Point Mass	Straight & Inelastic
Ranneberg (2013)	Square-root UKF	Position, tether force, tether length, steering input	Point Mass	Straight & Inelastic
Schmidt et al. (2017, 2020)	EKF	Position, velocity, wind speed and direction (reference height), tether force, tether length and reeling speed, steering input	Point Mass	Straight & Inelastic
Borobia et al. (2018); Borobia-Moreno et al. (2021)	EKF	Position, velocity, angular velocities, magnetic field, airspeed magnitude, tension at the bridles, kite center of mass	Rigid Body	Straight & Inelastic
Current Study	Iterated EKF	Position, velocity, tether force, tether reeling speed	Point Mass	Curved & Elastic (Quasi-Static)

60   tracking, which effectively reduced estimation errors under sagged conditions. However, these approaches do not estimate the wind velocity, which requires the inclusion of forces in the modelling to capture the wind impact on system behaviour.

In Williams et al. (2008), an unscented Kalman filter (UKF) was proposed as a state estimator for both the kite's state and wind conditions within a non-linear tracking control framework. The simulation results demonstrated that the UKF performed well when assuming a straight tether and was robust against noise. However, the wind velocity estimates were found to be the

65   most sensitive to noise.

Ranneberg (2013) utilized a UKF with a Lagrangian dynamic model that incorporates the forces on the kite, assuming constant aerodynamic coefficients, as well as rotational inertia of the drum. The results were validated against simulation data and experimental measurements, including pulsed lidar measurements at various heights, demonstrating that measuring the kite's position and the tether force is sufficient for estimating wind speed, although the vertical component of the wind velocity

70   was assumed to be zero. Schmidt et al. (2017, 2020) proposed a similar approach using an EKF with a Lagrangian dynamic model but without including drum inertia. Their model adds measured wind speed and direction at a reference altitude, which

works well for their case study of a kite flying at low altitudes but can introduce errors when the kite flies at higher altitudes. Nevertheless, the model is validated against experimental and simulation data, showing the potential of the approach.

In Borobia et al. (2018); Borobia-Moreno et al. (2021), a more complex model is employed to estimate the full state of the kite, including the ambient wind conditions and aerodynamic forces and moments. However, this increased complexity necessitates a significantly larger number of measurements. These measurements include data from GPS and IMU sensors, Pitot tube, including a five-hole Pitot tube, wind sensors on the ground and several load cells installed in the bridle line system of the kite.

A common limitation of existing methods is the assumption of a straight and inelastic tether, which can introduce errors when the tether force is low and the real tether sags. Additionally, soft kites with a suspended robotic control unit are affected by the inertia of the suspended unit, impacting orientation and dynamics (Roullier, 2020). Our study addresses these limitations by employing a more comprehensive model that accounts for both tether sag and KCU inertia, resulting in more accurate wind velocity estimates without requiring additional measurements. Specifically, we employ an iterated EKF that models the wing as a point mass and incorporates a quasi-static tether model (Williams, 2017). To account for the inertial effects of the KCU, an additional point mass is included between the tether and the wing, resulting in a two-point representation of the kite (Schelbergen and Schmehl, 2024). Validation through experimental data demonstrates the effectiveness of this approach in accurately estimating both wind velocity and kite state under varying atmospheric conditions. Although this study focuses on soft kites, the methodology is equally applicable to fixed-wing devices.

The results are presented for two kite prototypes, the V3 and the V9, both being leading-edge inflatable kites operated by Kitepower B.V., with flattened wing areas of 25 and 60 m^2, respectively. The V3 kite has been extensively studied in prior research and has served as a reference model (Oehler and Schmehl, 2019; Viré et al., 2022; Cayon et al., 2023; Poland and Schmehl, 2023; Schelbergen and Schmehl, 2024). In contrast, the V9 kite, representing Kitepower's current commercial prototype, is primarily used in the present study to showcase the method's ability to predict wind velocities at the kite. This analysis is based on an unprecedented dataset that combines high-quality AWES operational data with high-resolution wind measurements from profiling lidar. The AWES data include measurements of kite position, velocity, orientation, and accelerations; tether tension, length, and reeling speed; as well as airflow measurements from a Pitot tube and wind vanes, while the lidar data provide vertical wind profiles with good temporal and spatial resolution. Together, these datasets enable a comprehensive analysis of wind-kite interactions across various atmospheric conditions.

The remainder of this paper is organized as follows. Sect. 2 provides an overview of the AWE system, Sect. 3 discusses the experimental sensor setup, Sect. 4 details the filter design and sensor calibration, Sect. 5 presents the results and analysis, and Sect. 6 concludes with implications and future research directions.

2 System Overview

The main components of ground-generation soft kite AWESs are the ground station, tether, and kite, which consists of the wing, bridle system, and suspended kite control unit (KCU). The kite flies in cyclic patterns to generate electricity, alternating

between traction and retraction phases. During the traction phase, the kite performs crosswind manoeuvres, reeling out the tether and driving a drum connected to a generator. Once the tether reaches its maximum length, the system reverses, using the generator as a motor to reel in the tether while the kite is flown in a more aerodynamically efficient configuration to prepare for the next cycle.

In Fig. 1, the key components of a soft kite for airborne wind energy harvesting are shown alongside commonly used sensors. The kite is controlled by the KCU, which connects the bridle line system and the tether. The front bridle lines transmit most of the aerodynamic force from the wing, while the rear bridle lines are used to actuate the wing through the KCU and the steering and depower tapes. The steering tape deforms the wing asymmetrically by modifying the length of the steering lines to initiate turns, while the depower tape symmetrically adjusts the steering lines to pitch the wing relative to the KCU. This pitch is quantified by the depower angle α_d. Increasing this depower angle directly influences the kite's aerodynamic performance and is mainly used to reel in the kite efficiently.

The aerodynamics of the kite are generally characterized by the angle of attack at the centre section of the wing, α_w. However, directly measuring this angle is challenging because it would require isolating the inflow at the kite from the flow disturbances caused by its aerodynamics, which can be difficult to achieve reliably in practice. Consequently, sensors are more commonly installed on the bridle lines (see Fig. 3a) or on the tether below the KCU.

The bridle angle of attack α_b is defined as the angle relative to the plane perpendicular to the power lines and is related to the angle at the wing by

$$\alpha_\mathrm{w} = \alpha_\mathrm{b} - \alpha_\mathrm{d}, \tag{1}$$

where the depower angle, α_d, is approximated as a linear function of the depower input, u_p. This relationship includes an initial offset, $\alpha_\mathrm{d,0}$, corresponding to the powered kite state,

$$\alpha_\mathrm{d} = \alpha_\mathrm{d,0} + \Delta\alpha_\mathrm{d}\, u_\mathrm{p}, \tag{2}$$

where u_p ranges from 0 to 1, and $\Delta\alpha_\mathrm{d}$ represents the change in angle of attack from the fully powered to the depowered state. In previous works (Oehler and Schmehl, 2019; Schelbergen, 2024), this angle change was estimated using a simple geometric model that relates the length of the depower tape to the depower angle. However, with the integration of the tether model into the EKF, this angle can now be estimated directly from the measurements, as detailed in Sect. 5. Finally, the bridle angle of attack can be translated to the tether angle of attack, α_t, by

$$\alpha_\mathrm{t} = \alpha_\mathrm{b} + \lambda_0 + \theta_\mathrm{k}, \tag{3}$$

where λ_0 depends on the aerodynamic load distribution between the front and rear bridle lines, and θ_k is the kite pitch with respect to the tether caused by the KCU weight and inertia. λ_0 has been found to be relatively constant for a set depower setting but is highly dependent on changes in the depower tape length (Oehler and Schmehl, 2019).
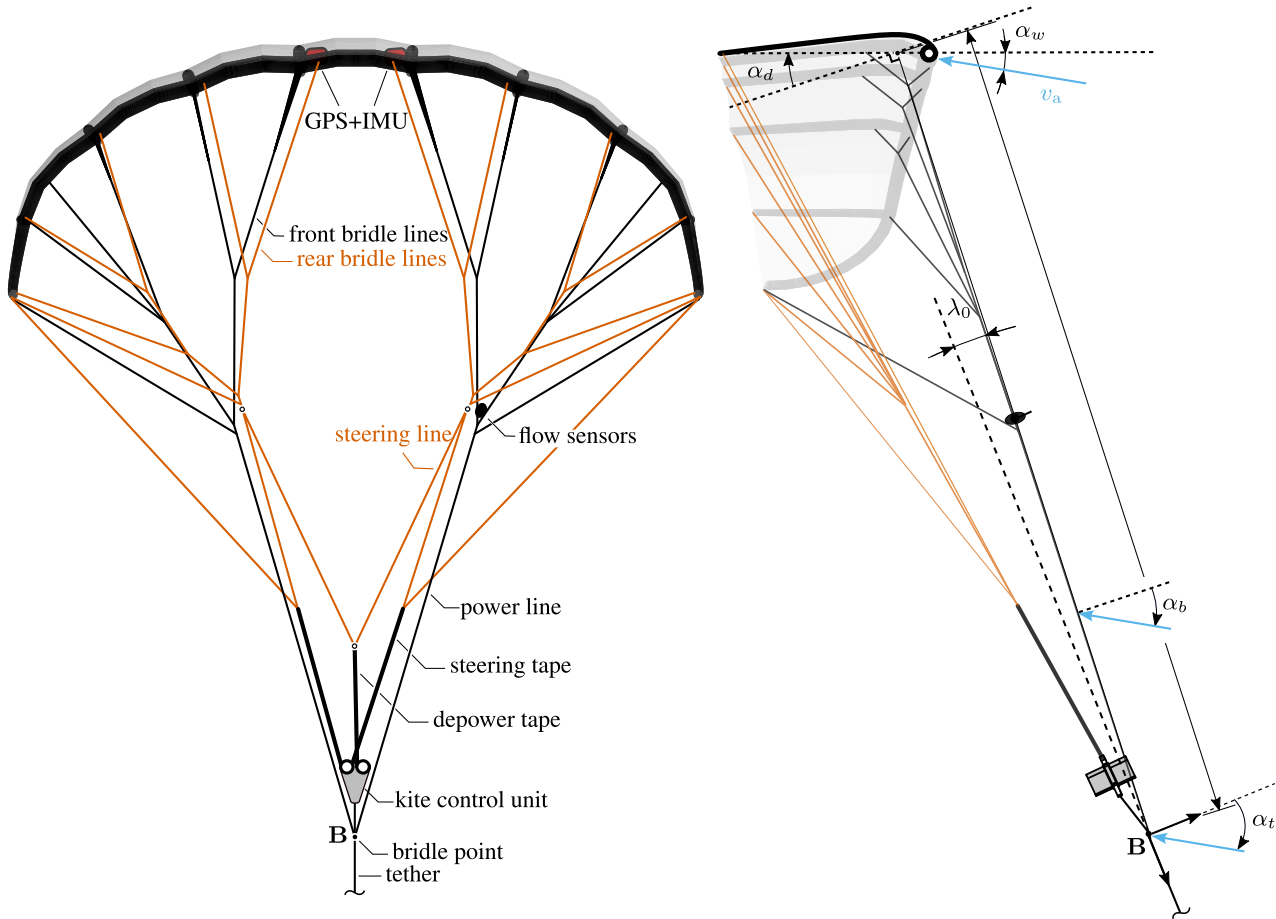
Figure 1. Illustration of system components and sensor setup. Adapted from Oehler and Schmehl (2019). The V3 kite geometry shows the bridle point **B** below the KCU, unlike the V9 geometry where the KCU is at the bridle point.

3 Sensor Setup

135

Measuring the state of AWESs presents significant challenges, particularly for soft kites, which, by their nature as tensile membrane structures experience substantial deformations during flight, along with vibrating components and high accelerations during turning manoeuvres. Understanding the accuracy and limitations of each sensor within its specific installation context is critical for developing an effective fusion technique. This understanding enables the design of a sensor fusion model relying

140 on the most trustworthy sensors.

The following is a breakdown of the key sensors used in the analysed datasets, along with a qualitative discussion of their advantages, limitations, and considerations for accurate measurements:

- Load Cells: The force exerted by the tether is measured using a load cell located at the tether exit point of the drum (see Fig. 2). This sensor can yield accurate results, provided it is correctly calibrated (Hummel et al., 2018). One could also consider installing load cells in the kite's bridle lines to measure the force distribution (Oehler et al., 2018; Borobia-Moreno et al., 2021). However, this approach significantly increases setup times and also the risks of failures and large inaccuracies in the measurements.

Figure 2. The V9 kite in flight: view from the ground station (left), and close-up showing the suspended control unit (right). Photos courtesy of Kitepower B.V.

- Tether length: The length of the tether is measured through the reeling mechanism of the kite, where an incremental angular encoder on the drum determines the rotational speed. From this, the deployed tether length is calculated (Vlugt et al., 2013). This method allows for accurate measurements, particularly if the initial offset of the tether length is correctly identified and accounted for.

- Tether angles: The elevation and azimuth angles of the tether can be measured at the ground station using magnetic angular encoders. When combined with the tether length, these measurements can be used to estimate the kite position (Peschel, 2013). The assumption of a straight tether generally holds during reel-out operations when the tether is under high tension, resulting in relatively accurate position estimates (Fagiano et al., 2013). However, the tether generally sags during reel-in due to reduced tension, leading to potential inaccuracies unless the sag is taken into account.

- GPS: The accuracy of GPS data is generally good as it is not affected by the deformation of the soft kite, making it a reliable source for position and velocity information. However, it is important to consider that GPS signals can be subject to problems such as signal loss, particularly during high acceleration manoeuvres (Vlugt et al., 2013).

Figure 3. Fully instrumented V3.25 kite before launch. Photo courtesy of Kitepower B.V.

160   – IMU: The placement of an IMU sensor on one of the inflatable tubes (see Fig. 3) of the kite has several implications. The sensor data is affected by the in-flight deformations of the wing, which are particularly noticeable when transitioning from powered to depowered states and during turns. These measurements of structural deformation are useful for assessing specific aspects of the wing deformation but can induce errors if used for trajectory estimations. Furthermore, the high accelerations of the kite during turns can lead to increased noise and sensor drift (Hesse et al., 2018).

165   – Wind Vanes: In the analysed setups, wind vanes were mounted in the bridle line system, where determining their orientation relative to the wing is challenging due to deformation of both the wing and the bridle lines. Furthermore, vibrations in the bridle lines can introduce noise into the measurements. Alternatively, these sensors could be mounted below the KCU, alleviating most of these issues. Ideally, these sensors would be integrated with an IMU for accurate measurements relative to the ground.

170   – Pitot Tube: Although Pitot tubes typically achieve good accuracy, they require regular maintenance and calibration, and external factors like ice, insects, or pollution can cause clogging (Ezzeddine et al., 2019). Furthermore, when used to measure wind speed, small errors propagate into larger errors due to the wind's small contribution to the total apparent

speed. Finally, the mounting position is critical; if the sensor is not mounted at the centre of rotation of the kite, it will measure velocity induced by the kite yaw rate, further amplifying inaccuracies.

175   Overall, the sensors that are least susceptible to the intrinsic deformations of the soft kite and the high accelerations of the system, and thus more reliable, are the GPS, the load cell (for tether force), and the mechanism measuring the tether length and tether angles. These sensors can maintain their accuracy despite the flexible nature of the kite. Consequently, the proposed sensor fusion model primarily relies on these measurements, resulting in a minimal sensor setup consisting of a GPS (for position and velocity), a load cell, and a tether length measurement. Furthermore, if the KCU inertia is modelled, a

180 measurement of the kite or KCU acceleration should also be included. In this study, due to data availability, this acceleration has been estimated by numerically differentiating the velocity. Additional measurements, such as airflow data or tether angles, are optional but can potentially enhance the accuracy of the estimations.

4   Filter Design

In this section, a filter is designed to estimate the state of a tethered flying system by integrating a dynamic model and an ob-

185 servation model in an EKF. The dynamic model captures the kite translational motion governed by aerodynamic, gravitational, and elastic tether forces. The tether dynamics are represented using a quasi-static lumped mass approach proposed by Williams (2017), expanded to include the effects of the KCU inertia and weight (Schelbergen et al., 2024). The observation model requires at least the position and velocity of the kite, as well as the tether force and reel-out speed as inputs. Additionally, to model the KCU inertia, a measurement of either the KCU or the wing acceleration should be included for accurate orientation

190 predictions. Its effect is accounted for by adding an extra tether segment to the model, representing the bridle line system, which connects to a point mass representing the KCU.

4.1 Dynamic Model

The dynamic model represents the kite wing as a point mass (m_{k}) following Newton's second law. Its acceleration results from the sum of the tether force at the kite $\mathbf{F}_{\mathrm{t,k}}$, aerodynamic force $\mathbf{F}_{\mathrm{a,k}}$, and weight $\mathbf{F}_{\mathrm{g,k}}$. The components of the aerodynamic force

195 are expressed as a function of the kite apparent velocity $\mathbf{v}_{\mathrm{a}}$ and the vector of aerodynamic coefficients $\mathbf{C}_{\mathrm{a}} = (C_{\mathrm{L}}, C_{\mathrm{D}}, C_{\mathrm{S}})$, which are assumed to be time-invariant,

$$\mathbf{F}_{\mathrm{a,k}} = \begin{cases} \mathbf{F}_{\mathrm{L}} = \frac{1}{2}\rho A_{\mathrm{k}} C_{\mathrm{L}} \|\mathbf{v}_{\mathrm{a}}\|^2 \mathbf{e}_{\mathrm{L}}, \\[2mm] \mathbf{F}_{\mathrm{D}} = \frac{1}{2}\rho A_{\mathrm{k}} C_{\mathrm{D}} \|\mathbf{v}_{\mathrm{a}}\|^2 \mathbf{e}_{\mathrm{D}}, \\[2mm] \mathbf{F}_{\mathrm{S}} = \frac{1}{2}\rho A_{\mathrm{k}} C_{\mathrm{S}} \|\mathbf{v}_{\mathrm{a}}\|^2 \mathbf{e}_{\mathrm{S}}, \end{cases} \tag{4}$$

where ρ is the air density, A_{k} is the projected area of the wing, C_{L}, C_{D}, and C_{S} are the lift, drag, and side-force coefficients, respectively, and $\mathbf{e}_{\mathrm{L}}$, $\mathbf{e}_{\mathrm{D}}$ and $\mathbf{e}_{\mathrm{S}}$ are unit vectors in the directions of the lift force, drag force and side-force, respectively. The

200 drag force acts in the direction of $\mathbf{v}_{\mathrm{a}}$, the lift force acts in the opposite direction of the tether force projected in the perpendicular

plane to $\mathbf{v}_\mathrm{a}$, and the side force acts orthogonally to both. The apparent velocity is a function of the kite velocity $\mathbf{v}_\mathrm{k}$ and the wind velocity $\mathbf{v}_\mathrm{w}$, which is also assumed to be time-invariant,

$$\mathbf{v}_\mathrm{a} = \mathbf{v}_\mathrm{w} - \mathbf{v}_\mathrm{k}. \tag{5}$$

The wind velocity can be accounted for using two different approaches: firstly, assuming it is time-invariant and not dependent
205   on height, and secondly, using a logarithmic relation with height for its horizontal component. The latter can be done by means of the friction velocity u_* and wind direction ϕ_w instead of the horizontal wind components such that the height-dependent horizontal wind speed $v_\mathrm{w,h}$ is given by (Watson, 2023),

$$v_\mathrm{w,h} = \frac{u_*}{\kappa} \log \frac{z}{z_0}, \tag{6}$$

where z is the height above the ground, $\kappa \approx 0.4$ is the von Karman constant and z_0 is the surface roughness length. Even though
210   this approach generally improves estimations by incorporating physical knowledge of the wind profile, it can lead to poorer estimations compared to modelling it as height-independent if the actual wind profile deviates from the assumed logarithmic model.

The tether force at the kite is determined by assuming a shape derived from a quasi-static force equilibrium, detailed in Williams (2017), with the addition of accounting for the KCU and its localised inertia, representing the kite by two separate
215   point masses (Schelbergen and Schmehl, 2024). The tether model uses a lumped mass approach with point masses connected by spring elements (see Fig. 4). The shape of the tether is calculated based on the tether force at the ground $F_\mathrm{t,g}$, the position $\mathbf{r}_\mathrm{k}$ velocity and acceleration $\mathbf{a}_\mathrm{k}$ of the kite wing, the wind velocity, the azimuth ϕ_0 and elevation β_0 of the first tether segment, and the total deployed tether length l, all of which are either incorporated into the dynamic model or directly measured and used as inputs.

220   The tether force at the wing is calculated using a shooting method, where the direction for each subsequent tether segment is determined by the sum of the elastic, drag, gravitational, and inertial forces given an initial estimate of the tether length and the tether force magnitude and orientation at the ground. Inertial forces for each segment are determined by their centripetal acceleration, with the segment lengths l_i adding up to the total tether length, including the bridle segment.

To compute these inertial forces, the velocities $\mathbf{v}_j$ and accelerations $\mathbf{a}_j$ of the discrete point masses along the tether are
225   estimated under the assumption that they all rotate with a fixed angular velocity $\boldsymbol{\omega}$, behaving like particles of a rigid body (see Fig. 5). The velocity at the the tether attachment point $\mathbf{B}$ particle can be represented assuming a purely rotational motion about a point, the instantaneous centre of rotation (Meriam et al., 2018), which is unique for each tether particle.

$$\mathbf{v}_\mathrm{B} = \boldsymbol{\omega} \times \mathbf{r}_\mathrm{c,B}, \tag{7}$$

where $\mathbf{r}_{\mathrm{c},B}$ is the vector from $\mathbf{B}$ to its instantaneous centre of rotation, which is perpendicular to $\boldsymbol{\omega}$. The acceleration can then
230   be estimated by differentiating the velocity,

$$\mathbf{a}_\mathrm{B} = \frac{d\mathbf{v}_\mathrm{B}}{dt} = \frac{d(\boldsymbol{\omega} \times \mathbf{r}_\mathrm{c,B})}{dt} = \frac{d\boldsymbol{\omega}}{dt} \times \mathbf{r}_\mathrm{c,B} + \boldsymbol{\omega} \times \frac{d\mathbf{r}_\mathrm{c,B}}{dt}, \tag{8}$$
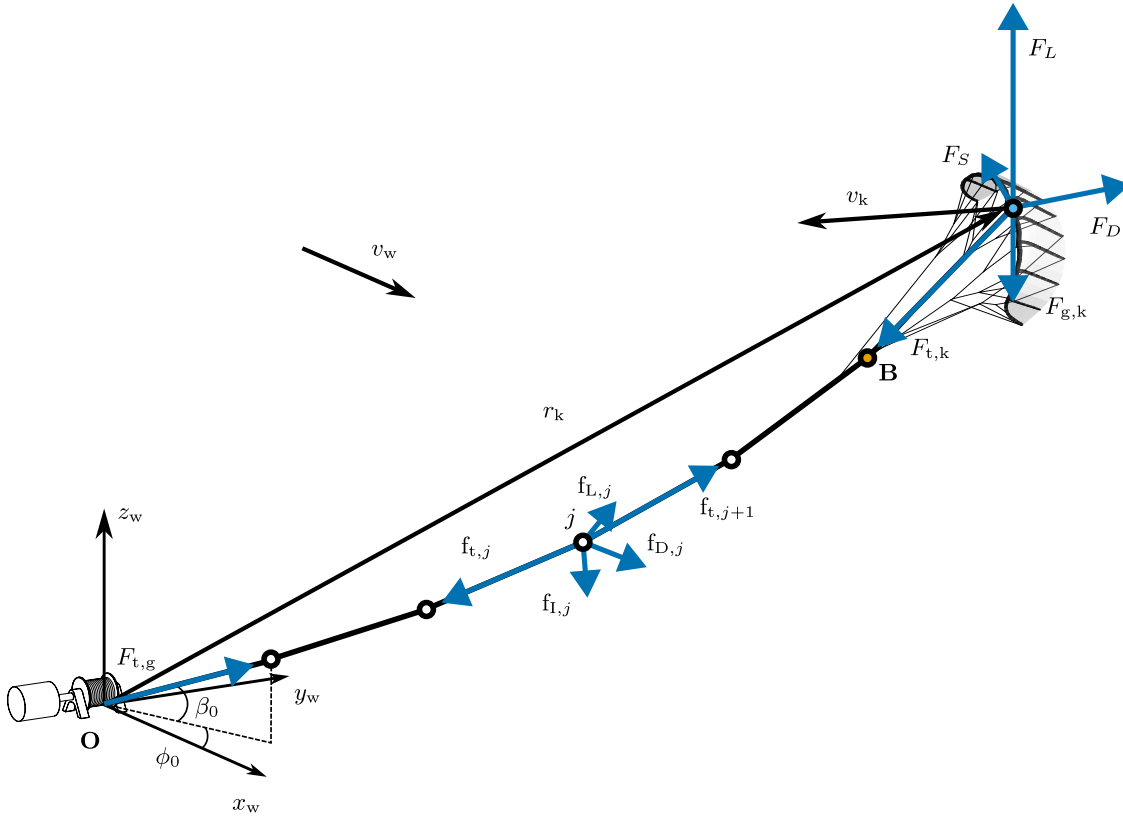
Figure 4. Schematic representation of the tether model and kite forces, as modelled by the dynamic system in the EKF. Adapted from Schelbergen and Schmehl (2024).

which can be expressed as,

$$\mathbf{a}_{\mathrm{B}} = \boldsymbol{\alpha} \times \mathbf{r}_{\mathrm{c,B}} + \boldsymbol{\omega} \times \mathbf{v}_{\mathrm{B}}. \tag{9}$$

Here, $\boldsymbol{\alpha} = d\boldsymbol{\omega}/dt$ is the angular acceleration. The two terms of the acceleration represent the tangential acceleration $\mathbf{a}_\tau = \boldsymbol{\alpha} \times \mathbf{r}_{\mathrm{c,B}}$ and the centripetal acceleration $\mathbf{a}_{\mathrm{n}} = \boldsymbol{\omega} \times \mathbf{v}_{\mathrm{B}}$.

235

If the acceleration and velocity of the tether attachment point **B** at the kite are known, we can compute the angular velocity, instantaneous centre of rotation, and angular acceleration as follows, assuming the tangential acceleration to be in the direction of the kinematic velocity,

$$\boldsymbol{\omega} = \frac{\mathbf{a}_{\mathrm{n}} \times \mathbf{v}_{\mathrm{B}}}{\|\mathbf{v}_{\mathrm{B}}\|^2}, \quad \mathbf{r}_{\mathrm{c,B}} = \frac{\mathbf{v}_{\mathrm{B}} \times \boldsymbol{\omega}}{\|\boldsymbol{\omega}\|^2}, \quad \boldsymbol{\alpha} = \frac{\mathbf{a}_\tau \times \mathbf{r}_{\mathrm{c,B}}}{\|\mathbf{r}_{\mathrm{c,B}}\|^2}. \tag{10}$$

240 On the straight flight path segments, the kite moves on a great circle trajectory, and $\boldsymbol{\omega}$ is perpendicular to the tether, resulting in the centre of rotation being located at the ground station along the extension of the tether (Schelbergen and Schmehl, 2024).
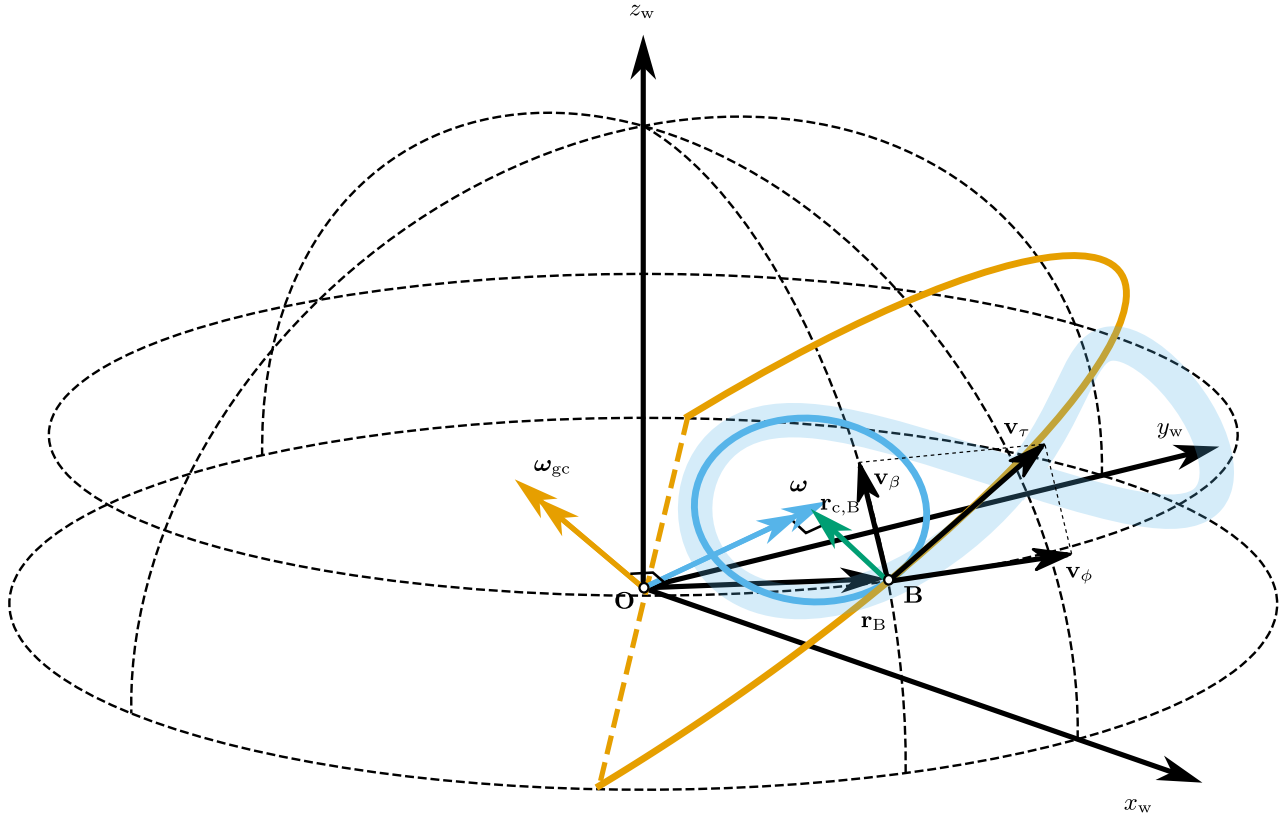
Figure 5. The angular velocity during straight flight, $\boldsymbol{\omega}_{\mathrm{gc}}$ (orange), and during turns, $\boldsymbol{\omega}$ (blue), for a kite linked by a straight and inelastic tether. Adapted from Schelbergen and Schmehl (2024).

However, during turns, the centre of rotation aligns with $\boldsymbol{\omega}$, and at each point along the tether, the centre of rotation will lie in the plane perpendicular to the angular velocity vector (see Fig. 5).

Given the angular velocity $\boldsymbol{\omega}$ and acceleration $\boldsymbol{\alpha}$, the velocity and acceleration at an arbitrary point 2 on the rigid body can
245   be determined relative to a reference point 1 as follows,

$$\mathbf{v}_2 = \mathbf{v}_1 + \boldsymbol{\omega} \times \mathbf{r}_{2-1}, \tag{11}$$

$$\mathbf{a}_2 = \mathbf{a}_1 + \boldsymbol{\alpha} \times \mathbf{r}_{2-1} + \boldsymbol{\omega} \times (\boldsymbol{\omega} \times \mathbf{r}_{2-1}), \tag{12}$$

where $\mathbf{r}_{2-1}$ is the position vector from point 2 to 1. The velocity at the ground tether attachment point is zero by definition of the system, which can also be confirmed as a direct result of these equations when applied to that point. Therefore, the
250   velocities and accelerations along the tether, relative to the ground point, can be written as,

$$\mathbf{v}_j = \boldsymbol{\omega} \times \mathbf{r}_j, \tag{13}$$

$$\mathbf{a}_j = \boldsymbol{\alpha} \times \mathbf{r}_j + \boldsymbol{\omega} \times (\boldsymbol{\omega} \times \mathbf{r}_j). \tag{14}$$

In practice, assuming the kite-tether assembly to be a rigid body can lead to inaccuracies. Firstly, the kite can rotate freely around $\mathbf{B}$[1], and secondly, the tether deforms and sags. As a result, the angular velocity vector $\boldsymbol{\omega}$ is no longer aligned with the

255 ideal rotation axis and does not pass through the ground station.

Initial attempts to model the assembly as a single rigid body yielded limited success, leading to the decision to treat the kite and tether as two independent rigid bodies. This approach significantly improved the estimations.

Since the kinematic measurements are obtained at the kite wing, the angular velocity of the kite, $\boldsymbol{\omega_k}$, is calculated using the accelerations and velocities at the wing (Eq. (10)),

260
$$\boldsymbol{\omega_k} = \frac{\mathbf{a}_{\mathrm{n,k}} \times \mathbf{v}_{\mathrm{k}}}{\|\mathbf{v}_{\mathrm{k}}\|^2}, \quad \mathbf{r}_{\mathrm{c,k}} = \frac{\mathbf{v}_{\mathrm{k}} \times \boldsymbol{\omega_k}}{\|\boldsymbol{\omega_k}\|^2}, \quad \boldsymbol{\alpha} = \frac{\mathbf{a}_{\tau} \times \mathbf{r}_{\mathrm{c,k}}}{\|\mathbf{r}_{\mathrm{c,k}}\|^2}. \tag{15}$$

Subsequently, the velocities and accelerations are translated to the bridle point $\mathbf{B}$, representing the KCU, using Eq. (11).

Regarding the tether, since the position, velocity, and accelerations at $\mathbf{B}$ are not measured, it is assumed to perform a great circle rotation around the ground station, which allows the angular velocity to be calculated using Eq. (13),

$$\boldsymbol{\omega}_{\mathrm{t}} = \frac{\mathbf{r}_{\mathrm{k}} \times \mathbf{v}_{\mathrm{k}}}{\|\mathbf{r}_{\mathrm{k}}\|^2}. \tag{16}$$

265 This assumption introduces inaccuracies, particularly in the acceleration values. However, since the point masses of the tether are relatively small, this does not significantly impact the overall accuracy of the model, as shown in Williams (2017). Assuming a constant angular velocity ($\boldsymbol{\alpha} \approx 0$), the velocities and accelerations along the tether are calculated as (Eq. (13)) (Williams, 2017),

$$\mathbf{v}_j = \boldsymbol{\omega}_{\mathrm{t}} \times \mathbf{r}_j, \tag{17}$$

270
$$\mathbf{a}_j = \boldsymbol{\omega}_{\mathrm{t}} \times (\boldsymbol{\omega}_{\mathrm{t}} \times \mathbf{r}_j). \tag{18}$$

The tangential velocity at the bridle point is then given by,

$$\mathbf{v}_{\tau} = \boldsymbol{\omega}_t \times \mathbf{r}_{\mathrm{B}}. \tag{19}$$

This tangential velocity vector is projected into the horizontal and vertical planes, yielding v_ϕ and v_β, to estimate the rate of change of the tether orientation angles.

275 The aerodynamic force acting on the tether is estimated based on the cross-flow principle, where the flow components parallel and perpendicular to the body are treated independently (Hoerner, 1965; Bootle, 1971), which was found to have a good relation with test data for sub-critical flows ($Re_{\mathrm{crit}} \approx 3.5 \times 10^5$), where the Reynolds number is formed using the tether diameter as the characteristic length. The lift $\mathbf{f}_{L,j}$ and drag $\mathbf{f}_{D,j}$ forces acting on each tether segment can then be estimated as follows (Dunker, 2018),

280
$$\mathbf{f}_{L,j} = \frac{1}{2}\rho \left(C_\perp \sin^2 \alpha_j \cos \alpha_j - \pi C_\parallel \cos^2 \alpha_j \sin \alpha_j \right) l_j d_t v_{\mathrm{a},j}^2 \mathbf{e}_{L,j}, \tag{20}$$

$$\mathbf{f}_{D,j} = \frac{1}{2}\rho \left(C_\perp \sin^3 \alpha_j + \pi C_\parallel \cos^3 \alpha_j \right) l_j d_t v_{\mathrm{a},j}^2 \mathbf{e}_{D,j}, \tag{21}$$

---

[1]In this work, we intentionally collocate the bridle point with the KCU for modelling simplicity. However, this was not the case for the V3 kite, as shown in Figs. 1 and 4, where the bridle point is slightly lower than the KCU.

where $C_\perp$ is the drag coefficient in the direction perpendicular to the tether, $C_\parallel$ is the skin friction drag coefficient (along the tether), α_j is angle of attack of the tether segment (which is $90°$ when the flow is perpendicular to the tether), l_j is the length of the tether segment, and d_t is the tether diameter. The direction of the drag force aligns with the apparent velocity of the segment, while the lift is directed perpendicular to the drag and lies in the plane defined by the apparent velocity and the tether direction, where $\mathbf{e}_{L,j}$ and $\mathbf{e}_{D,j}$ are unit vectors in the direction of these forces.

Similarly, the aerodynamic forces acting on the KCU are estimated by simplifying its geometry to that of a cylinder and applying the cross-flow principle, using experimentally derived coefficients for cylinders with different aspect ratios in the normal and tangential directions (Blevins, 1984), assuming the KCU is pitched $90°$ relative to the tether. However, since the KCU operates in a supercritical flow regime, the cross-flow principle may not provide an accurate approximation. A more suitable model for this regime is beyond the scope of the current project and will be considered in future work. Despite this, the contribution of the KCU drag to the overall system is very small compared to the other forces acting on the KCU and the system, so any inaccuracy here will not have a significant effect. This is further illustrated by the analysis presented in the results section.

The EKF state vector comprises the kite wing position and velocity, aerodynamic coefficients, wind velocity, tether length, and azimuth and elevation of the first tether segment. The tether length is determined by the reel-out speed (v_t), while the orientation of the first tether segment depends on its angular velocity relative to the ground station, which can be approximated with the tangential velocity and radial distance of the tether attachment point. The tether force at the ground $F_{t,g}$ is given as an input. With these considerations, the dynamics of the model can be written as a function of the state vector ($\mathbf{x}$) and the input vector ($\mathbf{u}$),

$$\mathbf{x} = (\mathbf{r}_k, \mathbf{v}_k, \mathbf{C}_a, \mathbf{v}_w, l_t, \beta_0, \phi_0), \qquad \mathbf{u} = (v_t, F_{t,g}). \tag{22}$$

The full system of ordinary differential equations (ODEs) to be solved is,

$$\mathbf{f}(\mathbf{x}, \mathbf{u}) = \begin{cases} \dot{\mathbf{r}}_k = \mathbf{v}_k & \text{(23a)} \\[6pt] \dot{\mathbf{v}}_k = \dfrac{\mathbf{F}_{t,k}\left(\mathbf{r}_k, \mathbf{v}_k, \mathbf{v}_w, l_t, \beta_0, \phi_0, F_{t,g}\right) + \mathbf{F}_{a,k}(\mathbf{C}_a, \mathbf{v}_w, \mathbf{v}_k) + \mathbf{F}_{g,k}}{m_k} & \text{(23b)} \\[6pt] \dot{\mathbf{C}}_a = 0 & \text{(23c)} \\[6pt] (\dot{\mathbf{v}}_w = 0) \quad \text{or} \quad (\dot{u}_* = 0, \quad \dot{\phi}_w = 0, \quad \dot{v}_{w,z} = 0) & \text{(23d)} \\[6pt] \dot{l} = v_t & \text{(23e)} \\[6pt] \dot{\beta}_0 = \dfrac{v_\beta}{\|\mathbf{r}_k\|} & \text{(23f)} \\[6pt] \dot{\phi}_0 = \dfrac{v_\phi}{\|\mathbf{r}_k\|}, & \text{(23g)} \end{cases}$$

Additionally, it is possible to estimate the offset in the measurements that are directly modelled, such as the tether length and angles, by adding them as a time-invariant variable ($\dot{\delta} = 0$).

This model forms the basis for the EKF design, capturing the essential dynamics of the kite and tether system. The model can be expanded to fly-gen systems by accounting for an additional thrust force acting on the kite, which can be modelled as

a function of the control inputs and the kite velocity. When added to Eq. (23b), the thrust can be an input or a state variable, depending on the EKF design.

4.2 Observation model

The required minimum measurements are the position and velocity of the kite wing. An additional observation is required to ensure that the position of the wing calculated with the tether model, $\mathbf{r}_{k,t}$, matches the estimated position of the kite wing, $\mathbf{r}_k$. This ensures an agreement between the position of the kite (Equation 23a) and the shape of the tether (defined by the tether length and the orientation of the first tether segment). Therefore, the observation model vector is given by,

$$\mathbf{h}(\mathbf{x},\mathbf{u}) = \begin{cases} \mathbf{r}_{k,m} = \mathbf{r}_k + \eta_{\mathbf{r}_k} & \text{(24a)} \\[4pt] \mathbf{v}_{k,m} = \mathbf{v}_k + \eta_{\mathbf{v}_k} & \text{(24b)} \\[4pt] \mathbf{0} = (\mathbf{r}_k - \mathbf{r}_{k,t}) & \text{(24c)} \\[4pt] \text{---optional---} \\[4pt] v_{a,m} = \|\mathbf{v}_w - \mathbf{v}_k\| + \delta_{v_a} + \eta_{v_a} \\[4pt] l_m = l + \delta_l + \eta_l \\[4pt] \beta_{0,m} = \theta_0 + \delta_{\beta_0} + \eta_{\beta_0} & \text{(24d)} \\[4pt] \phi_{0,m} = \phi_0 + \delta_{\phi_0} + \eta_{\phi_0} \\[4pt] \alpha_m = \alpha + \delta_\alpha + \eta_\alpha, \end{cases}$$

where the subscript m refers to the measured quantities, η_i represents the Gaussian-distributed measurement noise and δ_i the measurement offset for each variable i.

Additionally, several other measurements can be incorporated into the EKF to enhance its accuracy, such as the tether length, the orientation of the tether measured at the ground, the apparent wind speed, and the angle of attack, each potentially subject to an offset. However, it is important to recognize that poorly calibrated or faulty equipment can introduce significant errors in the estimation process.

4.2.1 Sensor Offset Correction

The EKF is designed to correct sensor biases, such as those in the tether length and angle measurements, by incorporating their offset as a state within the filter. This allows the filter to estimate and subtract the offset from sensor readings.

However, if the measurement is not directly modelled as a state variable, the filter may fail to estimate its offset accurately, requiring alternative methods. This problem is particularly relevant for airflow sensors like Pitot tubes and wind vanes. In such cases, a correction procedure is advised by initializing the filter without using the biased sensors. The estimated states are then used to calibrate the sensors after the filter has converged, provided the filter has been correctly pre-tuned to the system at hand.

Some measurements, such as the Euler angles from the IMU, are not directly modelled in the filter, and their offsets are corrected using the orientation of the bridle segment, which closely follows the measured orientation of the wing. However, if the IMU is positioned at the wing, the sensor will also measure the deformations due to the actuation. Larger deformations around the central strut of the wing are observed during reel-in and can be estimated based on the linear relationship between the variation in pitch and the de-power setting u_p, which is directly linked to the length of the de-power tape. By comparing the EKF-estimated pitch with the measured pitch θ_m, it is possible to infer the pitch sensor offset δ_θ and the de-power angle of attack α_d. This comparison allows the kinematic pitch of the kite θ_k to be isolated from the sensor readings:

$$\theta_\mathrm{k} = \theta_\mathrm{m} - \delta_\theta - \alpha_\mathrm{d} \tag{25}$$

The yaw angle, however, can only be estimated directly by incorporating the yaw rate into the filter model. Nevertheless, the anhedral shape of the kite naturally aligns it with the apparent wind, enabling an offset correction based on this tendency. The good agreement between estimations and measurements, along with the offsets for the Euler angles mentioned earlier, is presented in Sect. 5.

4.3 Extended Kalman Filter

In this section, the process followed by the iterated EKF to correct the measured states and predict the unknowns is described. This is illustrated in the flowchart in Fig. 6, where the hatted symbols denote the predicted states, and the superscript * represents the nominal state around which the EKF is linearised. The algorithm follows the standard setup of an iterated EKF (Gibbs, 2011) with a slight modification. After the one-step-ahead prediction, where the dynamic model is propagated to the next timestep, the Jacobians of the observation and dynamic model vectors are calculated. In this step, the tether force at the kite, obtained with the tether model, is differentiated only with respect to the tether length and the first tether segment orientation, whilst the rest of the states it depends on are taken from the last predicted state, given as input in the Jacobian calculation. There are several reasons for this choice; first, the tether model (Williams, 2017), in its original formulation, solves an optimisation problem for these three variables, while all the other variables are assumed to be known. Second, and more importantly, the introduction of the wind and kite velocity within the tether model introduces so much non-linearity that the performance of the Kalman filter is degraded. Therefore, the exact dependency of $\mathbf{f}$ on these states in the tether model is not accounted for when propagating the covariance matrices.

As shown in the remaining steps of the flowchart in Fig. 6, the iterated EKF follows a standard procedure to update its gain and state, as well as the covariance matrix of the state estimation error.

4.3.1 Tuning

One of the most crucial and complex aspects of a well-performing Kalman filter is tuning, which can be done by means of the state and measurement noise covariance matrices Q and R. For simplicity, these are defined as diagonal matrices, with the diagonal elements representing the expected variance of the state and measurement noise, assuming a Gaussian-distributed noise with zero mean. These matrices were found to be system-dependent, meaning their optimal values can vary between

1. One-step ahead prediction

$$\hat{\mathbf{x}}_{i+1,i} = \hat{\mathbf{x}}_{i,i} + \int_{t_i}^{t_{i+1}} \mathbf{f}\left(\hat{\mathbf{x}}_{i,i}, \mathbf{u}_i, t\right) dt \quad \rightarrow \quad \mathbf{x}^* = \hat{\mathbf{x}}_{i+1,i}, \ \mathbf{u}^* = \mathbf{u}_{i+1}$$

$$\bullet = \mathbf{x}^*, \mathbf{u}^*$$

2. Calculate Jacobians and discretize state transition matrix:

$$F_x(\bullet) = \frac{\partial}{\partial \mathbf{x}} f(\mathbf{x}(t), \mathbf{u}(t), \mathbf{x}^*, t) \quad \rightarrow \quad \Phi_{i+1,i}(\bullet)$$

3. Covariance matrix of state prediction error:

$$P_{i+1,i}(\bullet) = \Phi_{i+1,i}(\bullet) P_{i,i} \Phi_{i+1,i}^T(\bullet) + Q$$

4. Calculate Jacobian of measurement equations:

$$H_x(\bullet) = \frac{\partial}{\partial \mathbf{x}} h(\mathbf{x}(t), \mathbf{u}(t), \mathbf{x}^*, t)$$

$i = 1, 2, \ldots, N$

5. Kalman gain calculation:

$$K_{i+1}(\bullet) = P_{i+1,i}(\bullet) H_x^T(\bullet) \left[H_x(\bullet) P_{i+1,i}(\bullet) H_x^T(\bullet) + R_{i+1} \right]^{-1}$$

6. Measurement update:

$$\hat{\mathbf{x}}_{i+1,i+1} = \hat{\mathbf{x}}_{i+1,i} + K_{i+1}(\bullet) \left[\mathbf{z}_{i+1} - \mathbf{h}(\bullet) - H_x(\bullet)(\hat{\mathbf{x}}_{i+1,i} - \mathbf{x}^*) \right]$$

7. Check if converged:

$$\frac{\|\mathbf{x}^* - \hat{\mathbf{x}}_{i+1,i+1}\|}{\|\mathbf{x}^*\|} \leq \epsilon \quad \rightarrow \quad \mathbf{x}^* = \hat{\mathbf{x}}_{i+1,i+1}$$

No

Yes

8. Covariance matrix of state estimation error:

$$P_{i+1,i+1}(\bullet) = \left[I_n - K_{i+1}(\bullet) H_x(\bullet) \right] P_{i+1,i}(\bullet)$$

Figure 6. Iterated extended Kalman filter process flowchart.

different systems or kites. However, for the same kite, once calibrated, these coefficients maintain good performance even under varying environmental conditions.

The tuning of the EKF was performed manually, requiring an initial understanding of the magnitude and time dependence of the modelled parameters and a good knowledge of the accuracy of each sensor. There are, however, a few aspects that can be 365 checked to ensure proper calibration. The first is to ensure that the wind speed and direction estimates do not show any pattern-related variations, such as periodic changes due to the figure-of-eight pattern flown by the kite. Moreover, the filter estimates for position and velocity should closely align with the measurements. Finally, the aerodynamic coefficients should remain within the expected values of the flying wing. For a better understanding of the accuracy of the EKF estimates, analysing the time history of the filter performance parameters can be helpful. The normalized innovation squared (NIS) metric is commonly used
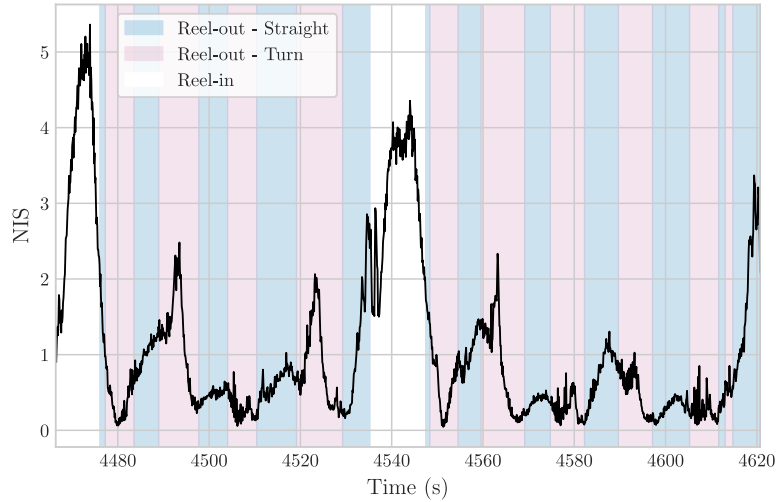
Figure 7. NIS metric for two power generation cycles.

370   for filter tuning in the absence of ground truth measurements (Bar-Shalom et al., 2002). It quantifies the consistency between the predicted measurements and the actual measurements, relative to the expected uncertainty.

$$\text{NIS} = \boldsymbol{\nu}_i^T \mathbf{S}_i^{-1} \boldsymbol{\nu}_i, \tag{26}$$

where $\boldsymbol{\nu}_i$ is the measurement residual and $\mathbf{S}_i$ the associated innovation covariance matrix.

    As shown in Fig. 7, the performance decreases during turns and reel-in, which may indicate either that the measurements

375   degrade during these phases or that the dynamic model cannot capture the relevant dynamics in these sections of the flight. Since position and velocity in the analysed datasets come from GPS+IMU-fused measurements, we believe the former to be the case, particularly during reel-in, as further discussed in the results section. For an optimally tuned filter, this metric should follow a chi-squared distribution; however, achieving this level of tuning is outside the scope of this work. For the leading-edge inflatable V3 kite, the standard deviations of the process and measurement noise terms detailed in Appendix A result in

380   reasonable estimates.

5   Results

The datasets used in this study were acquired during three test flights conducted by Kitepower in the frame of two test campaigns. The first campaign took place in 2019 at the former naval air base Valkenburg, the Netherlands, using the 25 m^2 V3.25B kite developed by Kitepower on the basis of the TU Delft V3 kite (Poland and Schmehl, 2024). The selected dataset was pub-

385   lished in Schelbergen et al. (2024) and analysed in Roullier (2020); Schelbergen and Schmehl (2024). It includes data from two sensor boxes with GPS+IMU mounted on the two central struts of the wing, an airflow sensor comprising a Pitot tube and a single wind vane measuring the angle of attack, a load cell on the ground, and tether length and reeling speed sensors.

Table 2. Overview of EKF models with corresponding sensor setups and wind model types.

Model	Additional Measurements	Wind Model
EKF 0	-	Constant
EKF 1	Tether length	Constant
EKF 2	-	Logarithmic
EKF 3	Apparent wind speed	Constant
EKF 4	Zero vertical wind speed	Constant
EKF 5	Tether length and angles	Constant

The second campaign took place 2023 to 2024 in Bangor Erris, Ireland, using the 60 m^2 V9 kite developed by Kitepower. This site in Northern Ireland is known for its consistently strong winds, predominantly from the south-west. The two selected flights of that campaign (Cayon et al., 2024a, b) include additional sensors used to study different measurement configurations. Measurement data was complemented with profiling lidar readings recorded using a Windcube v2 (Vaisala), which is used to validate the wind estimations of the EKF.

In this section, we explore various sensor setups and model configurations. The different EKF models are detailed in Table 2. The additional measurements listed in the table are used alongside the minimum required sensors for a system with a KCU, which include the position, velocity, acceleration of the kite wing, tether force, and reel-out speed.

The position and velocity data used in this study come from a GPS+IMU fused dataset processed with the embedded EKF of a Pixhawk sensor using PX4 autopilot. However, the fusion of GPS and IMU data can introduce inaccuracies, especially if the sensor fusion technique is not tailored to tethered flight.

5.1 Kite Kinematics

One of the primary functions of the EKF is to enhance the accuracy of existing measurements, such as the kite position and velocity. By integrating additional information, the EKF refines data from standalone kinematic sensors like GPS. In Fig. 8, portions of two flights from the two campaigns are depicted in terms of azimuth, elevation, and radial distance.

Overall, there is good agreement between the EKF estimations and the measurements throughout the flights. However, the highest discrepancies occur during the reel-in phase, when the kite is depowered, and to a lesser extent during turns. A significant factor contributing to these discrepancies is that the proprietary EKF of the Pixhawk relies on a model tailored to drones, which does not account for the constrained tethered flight dynamics of kites. This limitation likely contributes to inconsistencies in sensor readings, such as the mismatch between radial distance and tether length during reel-in, where the radial distance shows unphysical values several meters longer than the actual tether length. On the other hand, when the tether length is incorporated as an additional measurement, our EKF estimation aligns well with the tether length, correcting the position measurements to be consistent with the physical constraints of the system.
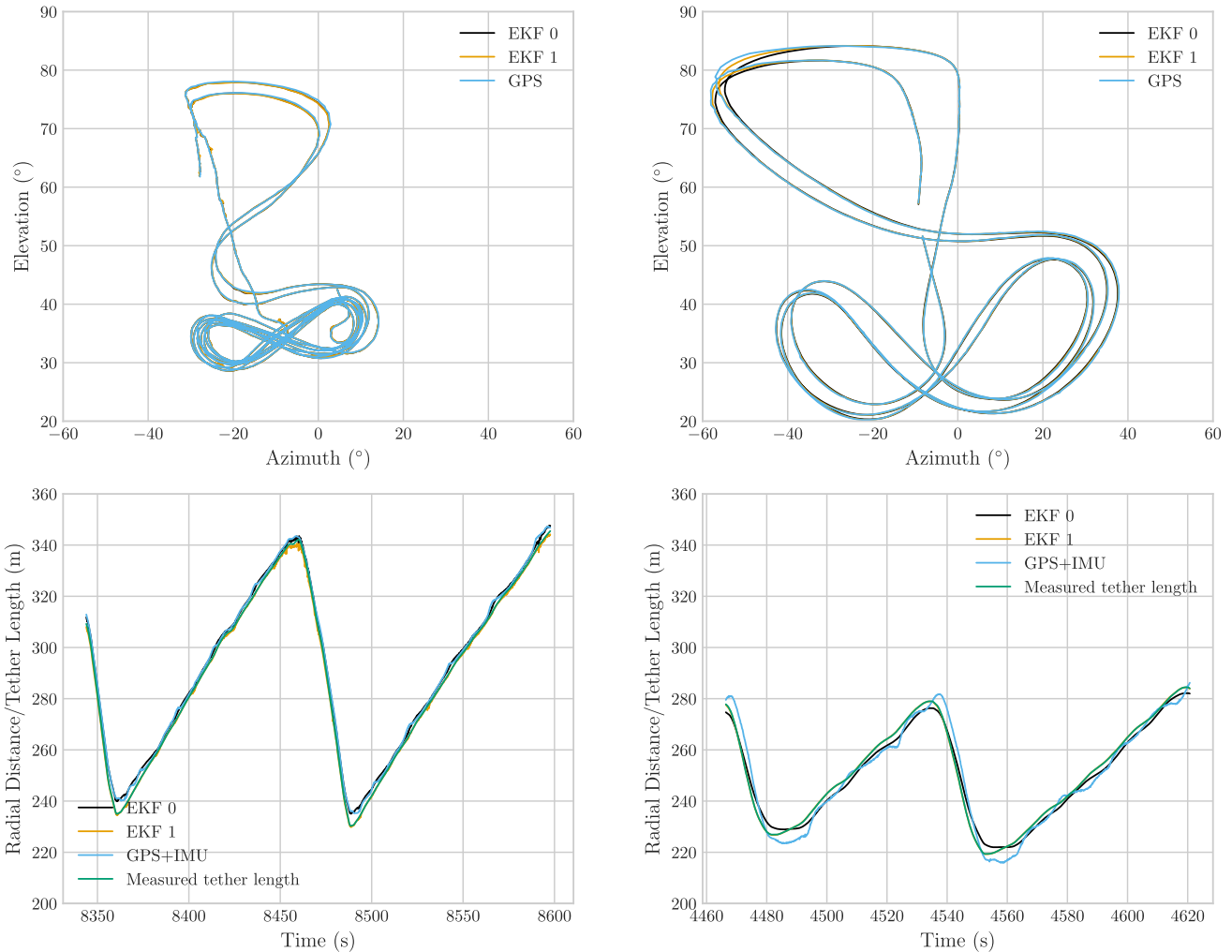
(a) V3 kite, flight 08-10-2019   (b) V9 kite, flight 27-11-2023

Figure 8. Comparison of estimated and measured kite trajectory, in terms of the azimuth and elevation angles and radial distance.

In Fig. 9, the Euler angles measured at the two central struts of the wing are compared with the orientation of the bridle segment, defined by a pitch and a roll. The third orientation angle, the yaw, is not modelled by the EKF and has been computed by aligning the kite reference frame either with the apparent wind or the kinematic velocity directions. As summarised in Table 3, the results show a strong agreement between the tether model and the orientation measurements from the IMU. This

415   level of consistency suggests that, for soft kites, a quasi-static two-point mass model—representing both the wing and the suspended KCU—can accurately capture the orientation of the kite.
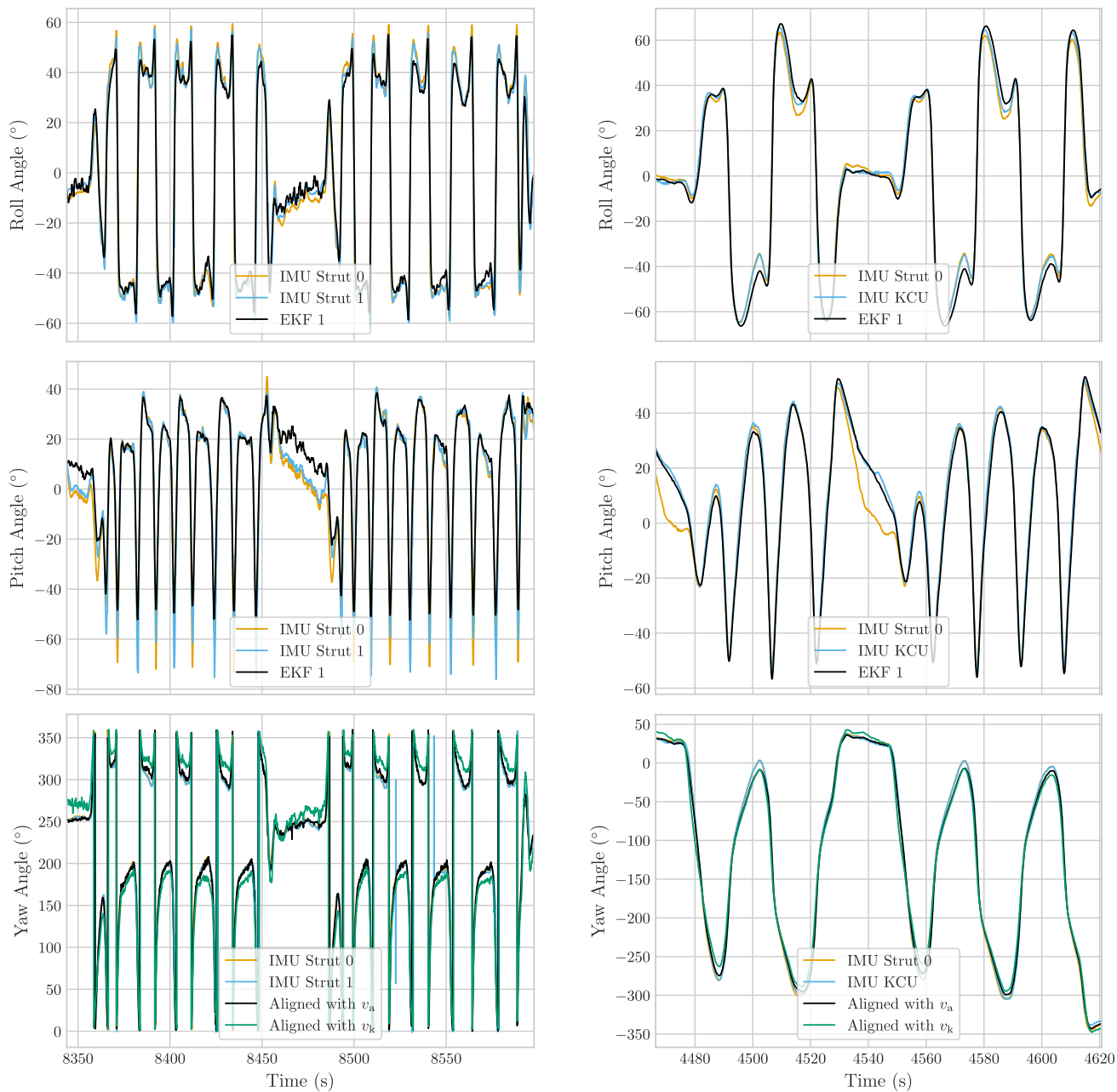
(a) V3 kite, flight 08-10-2019

(b) V9 kite, flight 27-11-2023

Figure 9. Comparison of estimated and measured Euler angles, with measurement biases removed using EKF estimations.

Furthermore, although yaw is not directly modelled, there is a notable alignment between the estimated and measured angles when the kite is aligned with the apparent wind direction. Conversely, the yaw estimation error increases when aligned with the kite kinematic velocity. This behaviour indicates that the kite's anhedral shape promotes alignment with the local inflow
420   rather than the kinematic velocity of the kite.

By modelling the tether shape, which includes the KCU, the kite deformation at the IMU can be estimated by comparing the predicted orientation of the bridle segment from the EKF with the measured orientations at the wing. This approach allows for an approximate assessment of wing deformation during flight and helps isolate the rigid body orientation.

Additionally, the model captures deformation effects that occur during changes in the depower setting and turning manoeu-
425   vres. For instance, the depower-induced deformation is evident in Fig. 9, where a pitch change of approximately 9° is observed for the V3 kite during reel-in. This information can be utilised to translate the measured angle of attack at the bridle to the wing angle of attack (see Eq. 1).

Regarding turning deformation, this effect is most pronounced in the V3 kite (see Fig. 9a), which corresponds to a kite whose structure exhibited greater overall deformation. Such deformation may be undesirable if the goal is to maintain aerodynamic
430   performance. However, this clear identification of turning deformation, which is more pronounced in one strut than the other depending on the turning direction, provides valuable insight into the aero-structural deformations of the wing (Schelbergen and Schmehl, 2024).

Table 3. Root mean squared errors (RMSE) of pitch, roll, and yaw for two kite models

Orientation RMSE	V3 (2019-10-08)	V9 (2023-11-27)
Pitch	3.63 deg	3.07 deg
Roll	3.84 deg	2.91 deg
Yaw (aligned with v_a)	4.15 deg	4.65 deg
Yaw (aligned with v_k)	13.43 deg	11.73 deg

5.2   System dynamics

Modelling the various components of the kite and tether system allows for the isolation of individual force components,
435   enabling an assessment of their relative significance. Fig. 10 illustrates the different forces acting on the V3 kite system.

As expected, the lift force generated by the wing is the dominant contribution, primarily responsible for pulling the tether. It is followed by the wing drag force, which exhibits considerable variability, peaking during turns and decreasing during the reel-in phases. The parasitic drag of the tether and KCU can be seen to account for a relatively small portion of the total drag. The side force, though relatively low, plays a crucial role in balancing the forces during turns by providing the necessary lateral
440   force to counteract the centripetal acceleration of the wing. The primary force component of the KCU is its inertia, which can be interpreted as an external force on the tether. In this particular system configuration, where the KCU was oversized relative

to the wing, its inertia could reach up to 40% of the tether force during turns, exerting a greater influence than its weight due to the high accelerations during turns.
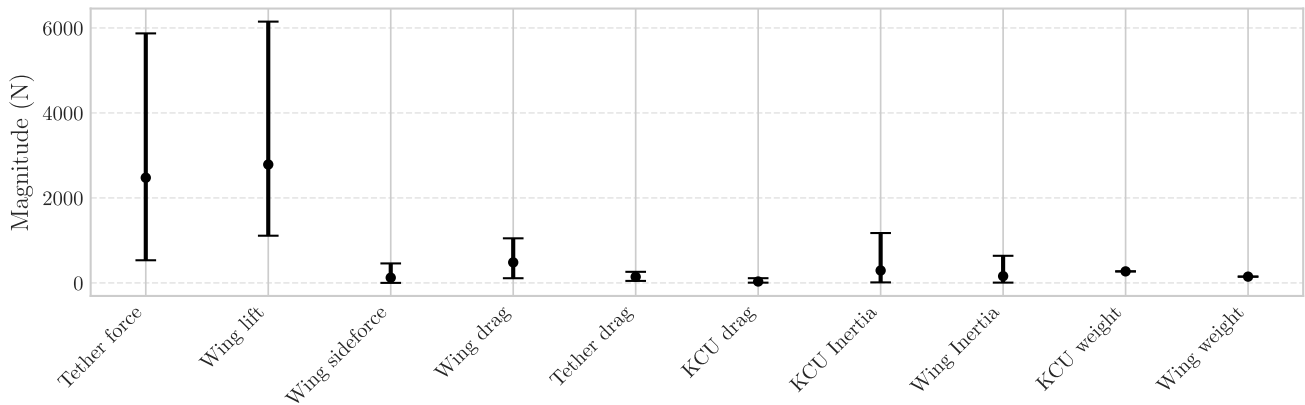
Figure 10. Mean, maximum, and minimum values of the different force contributions acting in the airborne subsystem during the flight on 2019-10-08 using the V3 kite.

Another novelty is that the current EKF can effectively estimate tether sag, understood as the difference between the radial 445 distance and the tether length. Fig. 11 presents the sag and ground tether force for two power generation cycles, revealing a clear relationship between the two. As expected, the tether experiences the most sag during the reel-in phases, when the kite is depowered, and the tether forces are lowest.
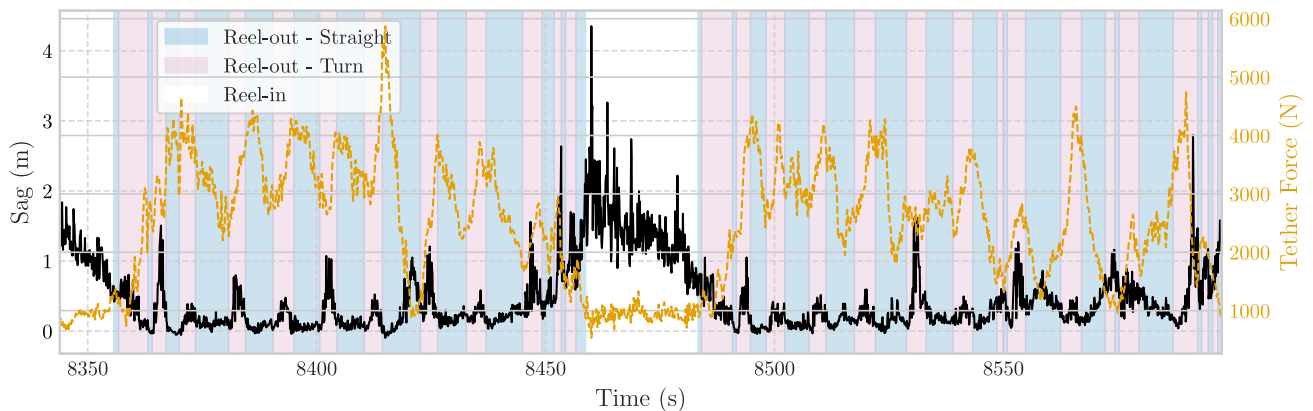
Figure 11. Variation of sag and tether force during two power generation cycles from the flight on 2019-10-08 using the V3 kite. The plot shows the sag in meters (left y-axis) and the tether force in Newtons (right y-axis).

Additionally, a consistent peak in sag is observed during turns, partly due to the reduced speed at the top of the figure-eight pattern (i.e., lower tether force). This effect is further amplified by the inertia of the KCU, which causes the kite to rotate relative to the tether. This misalignment between the aerodynamic forces and the tether force might lead the kite to dive into the sphere, causing the tether to sag.

Aerodynamic identification

To accurately estimate the aerodynamic performance of the kite, it is crucial to precisely estimate both the orientation of the tether and the wind speed and direction. The latter is particularly critical for determining the direction of the drag force and obtaining accurate estimates of the drag coefficient. Linking the instantaneous aerodynamic coefficients to the angle of attack at the wing α_{w} adds another layer of complexity, as this angle is currently measured at the bridle. This section aims to improve the accuracy of these estimates by integrating deformation estimates from the EKF to calculate the angle of attack at the wing, thereby enhancing the prediction of the wing aerodynamic coefficients as a functions of the angle of attack.

Alternatively, the angle of attack can be calculated using the orientation of the wing measured by the IMU and the estimated apparent wind velocity. However, the accuracy of this method is limited by the time resolution quality of the wind velocity estimates, making the measured angle of attack better at capturing temporal variations. Nevertheless, this angle is used to find $\alpha_{0,\mathrm{d}}$, which is subtracted from the measured angle at the bridle (see Eq. (1)),

In Fig. 8a, the measured trajectory of two power generation cycles is presented alongside the EKF estimates, with the azimuth angle centered on the mean wind direction. During this flight segment, the trajectory was slightly misaligned with the wind direction by approximately $10°$, according to the EKF predictions.

In Fig. 12, the aerodynamic coefficients and angles of attack are plotted for the selected flight segment. The lift and drag coefficients remain relatively constant throughout the reel-out phase, with spikes during turns corresponding to decreased lift and increased drag. Additionally, the side of the figure-eight pattern that is more misaligned with the wind direction shows a higher increase in drag coefficient and a smaller decrease in lift, while on the other side, the drag peaks are smaller, and the decrease in lift is higher. The increase in drag coefficient on the misaligned side of the figure of eight pattern could be attributed to a higher sideslip angle, although relating this directly to the lift coefficient is less straightforward. The observed changes in lift might be linked to variations in the kite's trim angle, which could be influenced by shifts in aerodynamic polars with sideslip, although this relationship warrants further investigation.

The parasitic drag of the tether and KCU contributes a significant portion of the total drag, approximately 30% during reel-out and up to 50% during reel-in. As for the angles of attack, the measured angle at the bridle lines remains fairly constant throughout the flight, suggesting that the kite maintains pitch stability around a certain trim angle (Thedens and Schmehl, 2023; Cayon et al., 2023). The angle measured at the bridle lines can be translated to the wing angle of attack using the depower-induced deformations identified in Fig. 9a.

The wing polars using this estimated angle are presented in Fig. 13 as mean values, with shaded areas indicating the 99% confidence interval. As inferred from the angle of attack and aerodynamic coefficient estimates shown in Fig. 12, the kite exhibits relatively constant behaviour for a fixed depower setting, which limits the range of angles of attack explored during
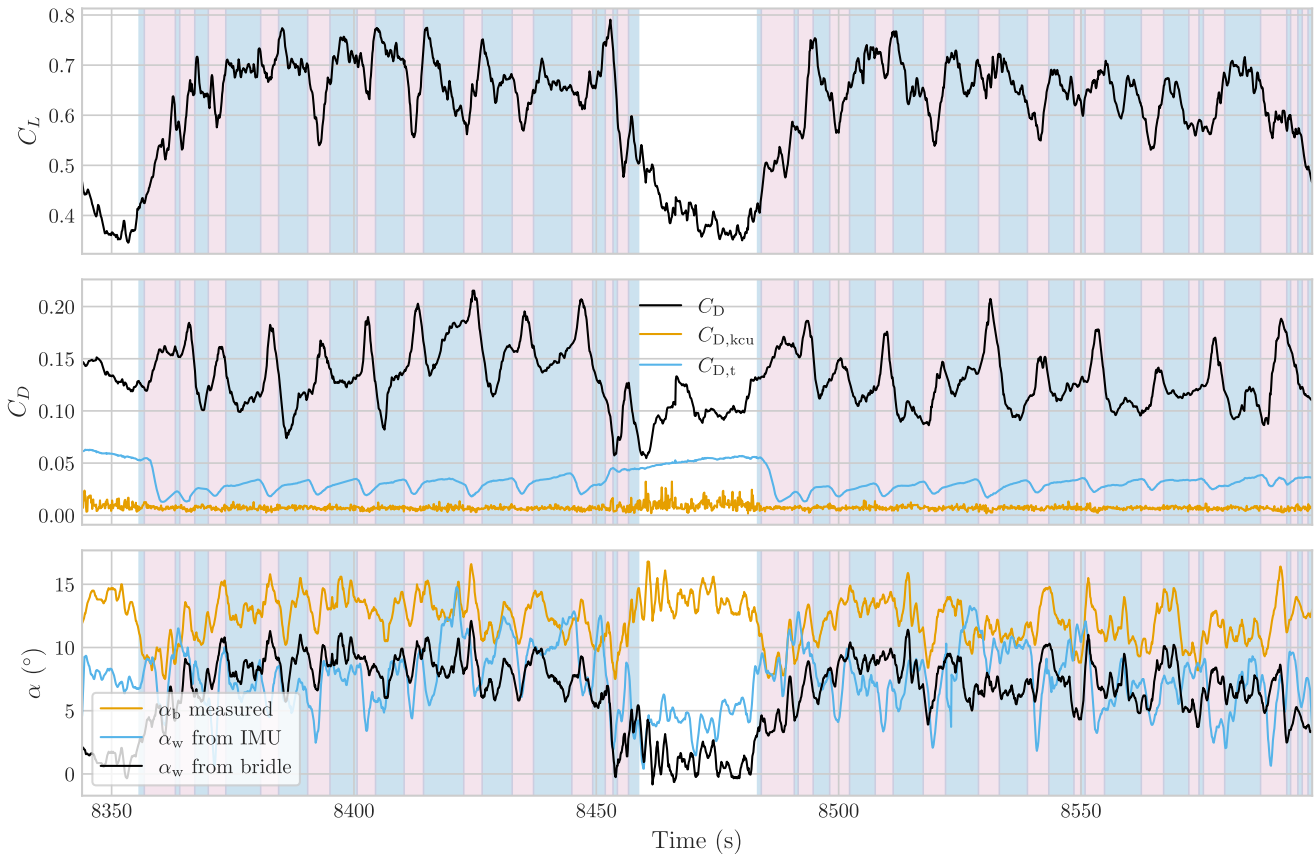
Figure 12. Aerodynamic coefficients and angle of attack of the V3 kite during two power generation cycles. The background colours indicate the flight phase of the kite, legend can be found in Fig. 11.

this flight. Despite this constraint, portions of the polar curves can still be estimated. However, for a complete aerodynamic characterisation of the kite, tailored test flights should be conducted, where the kite is forced to dynamically change the angle of attack to explore the wider range of conditions. The experimentally derived polars are compared with findings from

485 previous studies employing different levels of fidelity. The Reynolds-Averaged Navier-Stokes (RANS) simulations by Viré et al. (2022) were conducted using the CAD model of the V3 kite, whereas the results from the Vortex Step Method (VSM) incorporate an aero-structural solver that accounts for kite deformation caused by actuation inputs (Cayon et al., 2023; Poland and Schmehl, 2023). Additionally, the estimations are compared with an experimental study of the same dataset that used a simpler tether model (Roullier, 2020). In this study, the wind speed at the kite was extrapolated from ground measurements

490 using a logarithmic wind profile, and the angle of attack was estimated based on geometric relations rather than experimentally identified deformations.
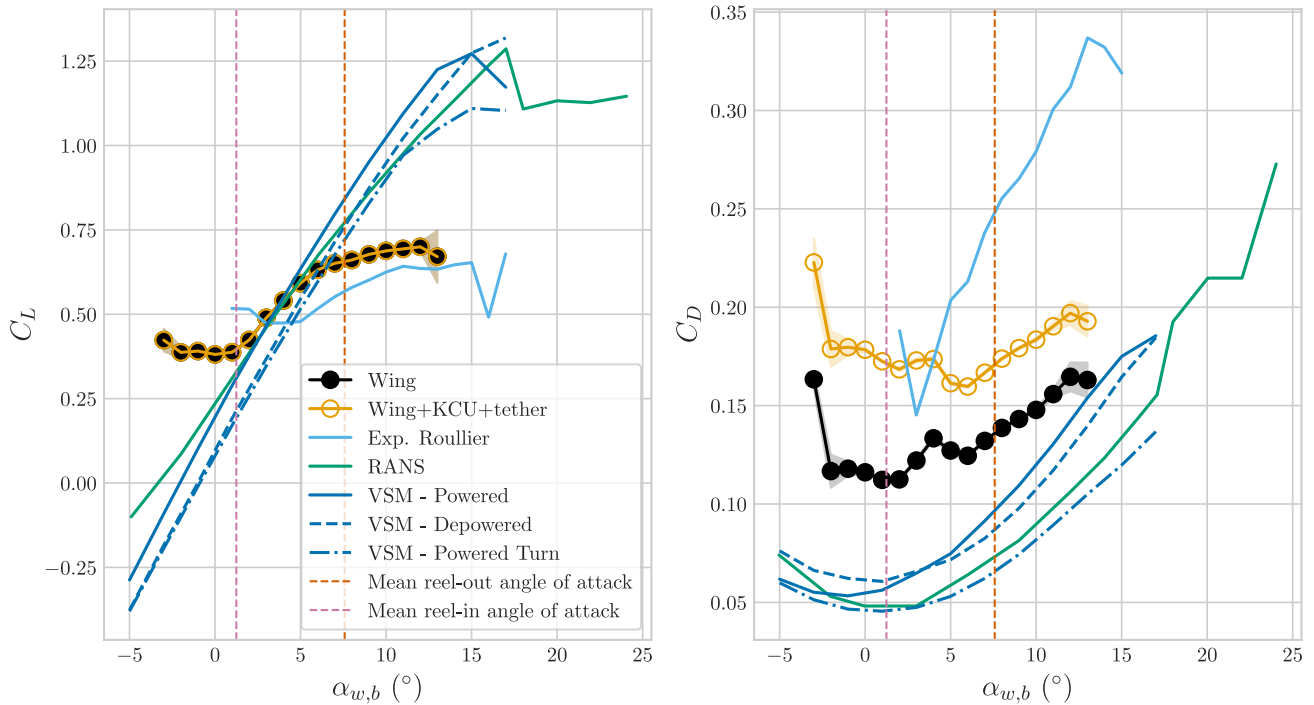
Figure 13. Aerodynamic polars of the V3 kite on the flight of 08-10-2019.

Compared to the RANS simulations of the constant design wing shape, a similar lift slope is observed between the mean angles of attack in powered and depowered states, consistent with the VSM results. However, the behaviour around the mean angle of attack is flatter than in the previous simulations. This flattening can be attributed to two main factors. First, the angle
495 of attack measurements have an accuracy of approximately 2° and are subject to vibrations, introducing noise that smooths the curve around the trim angle of the kite during reel-out. Second, the aerodynamic performance of the kite is significantly influenced by steering-induced deformations, which may alter the polars.

When comparing these results to the experimental analysis by Roullier (2020), the derived polars exhibit a closer resemblance to the simulations, largely due to improvements in both angle of attack and wind vector estimations. Additionally, by
500 modelling the drag of various parasitic elements in greater detail, a curve with lower drag coefficients and higher lift coefficients is identified.

Turn dynamics

To steer the kite, a lateral force is generated by asymmetrically deforming the wing, controlled by the steering input u_s via actuation of the steering tape. This deformation creates a lift difference between the two sides of the wing, producing a net

lateral force that steers the kite and a moment that induces yaw. Therefore, we can broadly characterise the turning behaviour by the side-force coefficient C_S and the yaw rate $\dot{\psi}$.

For soft kites, where turns are predominantly induced by aerodynamic forces at the wing tips, the yaw rate can be described by a simple relationship dependent on steering input u_s and the apparent wind speed v_a (Fagiano and Novara, 2014; Erhard and Strauch, 2012). This relationship suggests equilibrium of the aerodynamic moment during turns and is expressed as:

$$\dot{\psi} = g_\mathrm{k} v_\mathrm{a} \left(u_\mathrm{s}(t - d(t)) - u_{\mathrm{s},0} \right), \tag{27}$$

where g_k is the steering gain parameter, $u_{\mathrm{s},0}$ is an offset observed in the side-force coefficient estimates (Fechner, 2016), and $d(t)$ is the time delay between the steering input and the kite response (Elfert et al., 2024).

A time delay of approximately 0.1 seconds is observed when cross-correlating the yaw rate with the steering input, while the delay for the side-force coefficient is around 0.8 seconds relative to u_s. Understanding these delays is crucial for improving the kite responsiveness and steering precision. Further investigation is needed to determine whether these delays originate from the filter dynamics or the physical response of the kite.

In Fig. 14, the kite turn dynamics are depicted in terms of yaw rate and side force coefficient. The identified yaw rate closely matches the measured values, particularly when the offset in the steering input is accounted for. The largest discrepancies occur during straight flight sections and reel-in phases, where the kite is minimally steered. Nevertheless, as shown in Fig. 15, the yaw rate of the kite is well represented across all flight conditions by a simple turn rate law.

For the side-force coefficient, a linear relationship is fitted between the steering input and side force, providing accurate estimates during turns. However, during straight paths, a notable mismatch arises, where the side force appears to be consistently underpredicted, indicating that the same linear fit might not be suitable for all flight regimes.

This is further illustrated in Fig. 16, which shows the side force as a function of u_s. The data highlight distinct behaviours during turns and straight flight, with changes in side force due to the steering being more pronounced during straight flight. This phenomenon can be attributed to aerodynamic damping caused by the wing's yaw motion, which results in the outer side of the kite moving at a higher velocity relative to the inner side. Consequently, the force generated by the turn opposes the manoeuvre, altering the rate of change of C_S with respect to u_s.

Beyond the direct effects of steering input on turn dynamics, it is also essential to consider how other components, such as the KCU, influence the overall system behaviour. By modelling the kite and KCU separately, it is possible to assess the effects of KCU inertia on the manoeuvrers and performance of the kite system. In Fig. 17, the estimated angles between the tether and the kite, defined by the orientation of the bridle segment, are shown for two power generation cycles. It is important to note that in the flight shown, the KCU was significantly oversized compared to the kite, with its weight reaching twice that of the wing itself. As a result, the behavior observed is exaggerated compared to what would be expected in an optimised system. Nevertheless, this exaggerated scenario provides clearer insights into the effects of the KCU on the system.

During reel-out, the pitch angle remains relatively low, while the roll angle oscillates between positive and negative values, depending on the direction of the kite. During turns, where the accelerations are highest, a peak is observed in both the roll and pitch angles caused by the centrifugal force acting on the KCU. On the straight path segments of the figure eight manoeuvres,
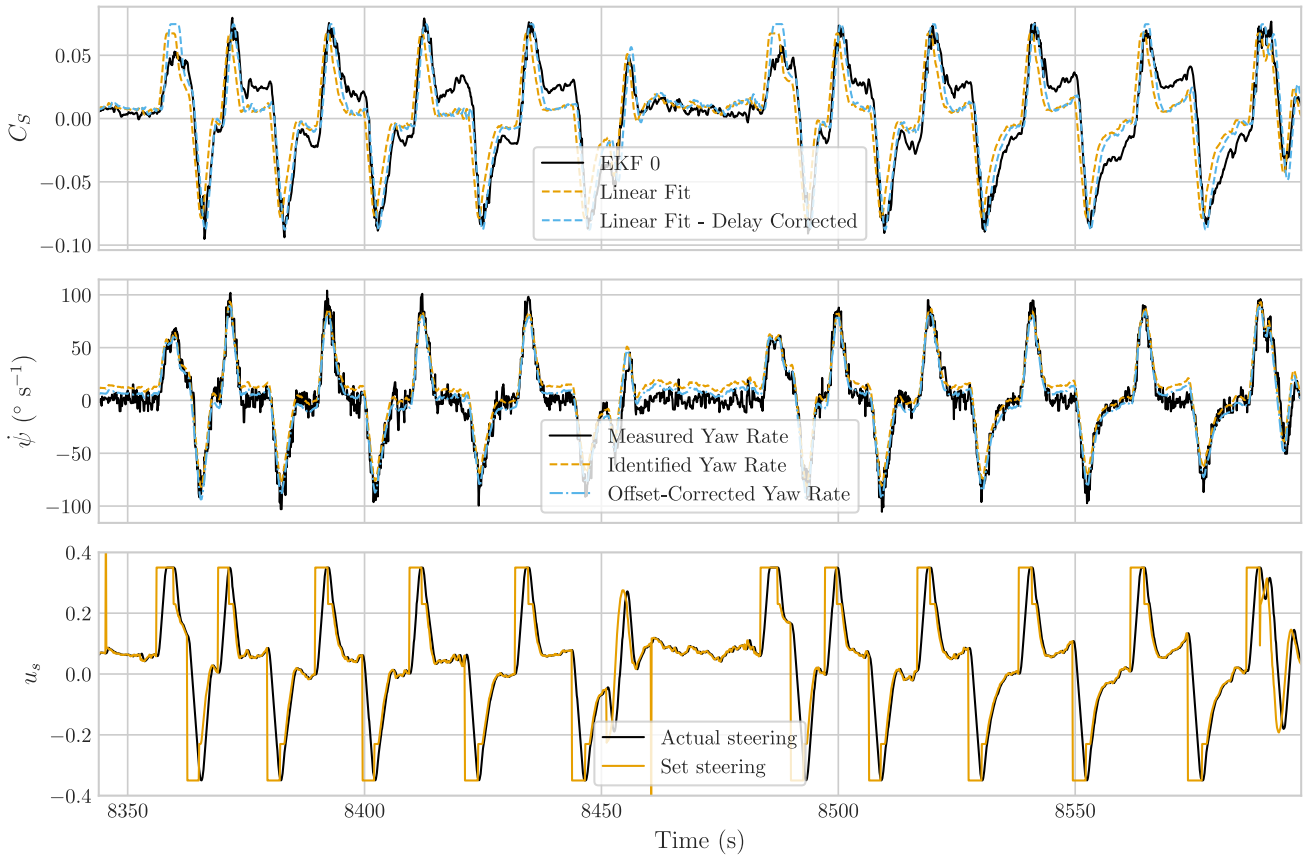
Figure 14. Side force coefficient, yaw rate, and steering input for two power generation cycles.

the roll angle has a lower value, primarily compensating for the weight of the KCU. However, when the kite is reeled in, due
540 to the orientation change toward the ground station, the weight of the KCU is compensated mainly by the pitch angle.

This misalignment of the kite with respect to the tether means that a portion of the aerodynamic force generated by the kite
is not transmitted as tether tension but is instead used to compensate for the inertial forces at the KCU. In this exaggerated
scenario, these losses can reach up to 6% during turns, highlighting the significant impact of the KCU mass on the system
performance Roullier (2020).

545 **5.3 Wind Estimations**

In this section, we present results from two selected flights of the more recent flight campaign in Ireland. The 2023-flight
exhibits a typical logarithmic wind profile, while the 2024-flight displays a transient phenomenon characterised by a sudden
wind gust and a rapid change in wind direction. Estimates relying on a logarithmic law were obtained assuming a surface
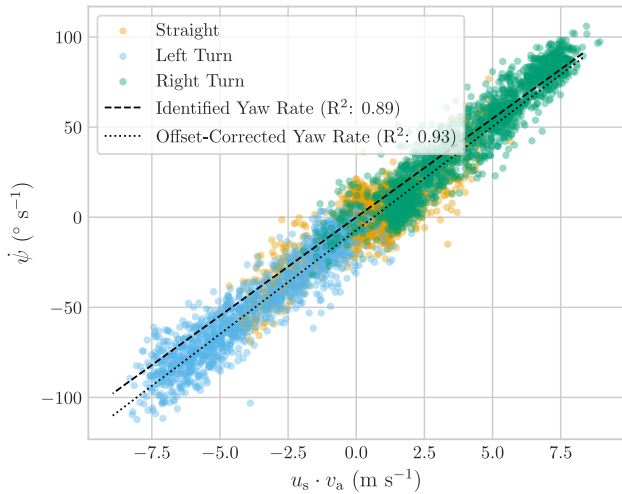
Figure 15. Measured yaw rate and identified turn rates with and without offset correction.
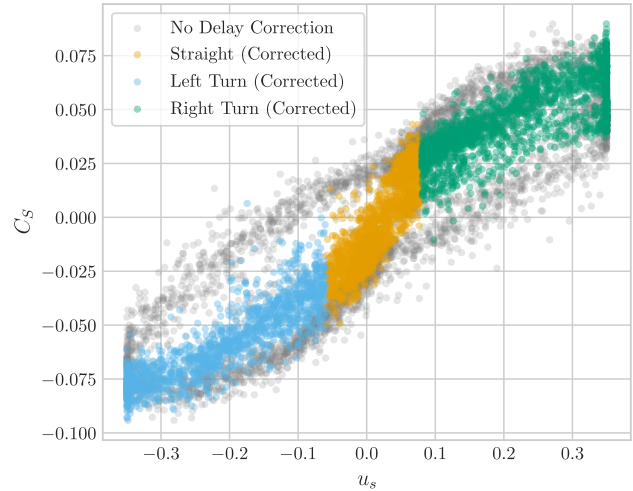
Figure 16. Sideforce coefficient as estimated by the EKF with and without correcting the time delay.
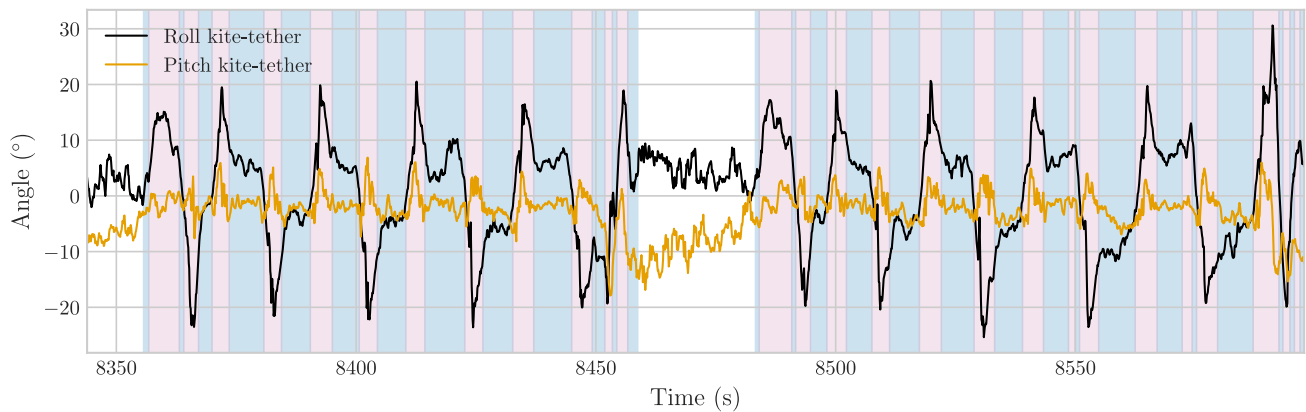
Figure 17. Estimated angle between tether and kite for the V3 kite during two power generation cycles. The background colors indicate the flight phase of the kite, legend can be found in Fig. 11.

roughness length z_0 of 0.1 m. Below, we introduce these two flights and provide a detailed commentary on the wind speed and

550   direction estimates.

   For the 2023-flight, Fig. 18 shows a comparison between the wind speed and direction profiles and the results of several EKF model configurations with different sensor measurements as inputs. Ground wind measurements from a cup anemometer and wind vanes were also available for that flight, with the wind speed extrapolated to the kite height using a logarithmic wind profile (see Equation 6). Likewise, lidar data collected at different fixed heights was interpolated to the kite altitude, with

555 shaded areas indicating the range between minimum and maximum values. The lidar data consist of one-minute averages, with

the minimum and maximum values showing variability within each averaging period.
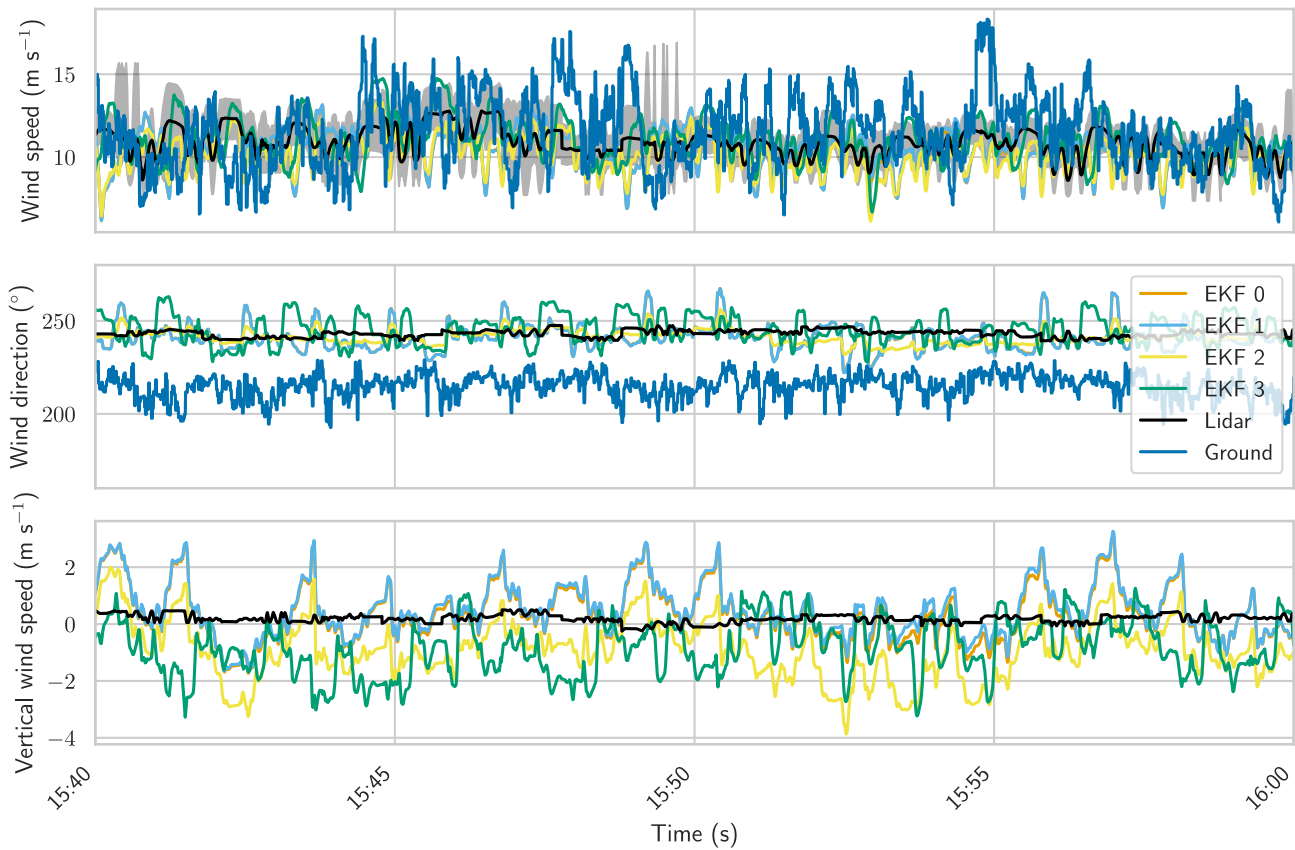
Figure 18. Test flight from 27-11-2023. Time series comparison of different EKF model results and lidar observations and ground measurements.

The results show strong agreement across all configurations for both wind speed and direction. For this flight, incorporating

the tether length as a measurement (EKF 1) does not lead to significant changes in the wind estimates. By modelling wind

speed as logarithmically dependent on height (EKF 2), it is possible to tune wind speed and direction separately, allowing

560 for independent control over their fluctuations. This approach reduces variability in wind direction while maintaining a clear

dependence of wind speed on height.

The highest fluctuations in wind direction are observed when the apparent wind speed is included as a measurement (EKF 3).

However, it is challenging to determine whether these fluctuations are physical or the result of errors in the Pitot tube readings,

especially when compared against the lidar's 1-minute average data. A poorly calibrated tube or its position away from the

565 centre of rotation of the kite might cause these fluctuations. For this flight, the Pitot tube readings were corrected using the methodology described in Sect. 4.2, resulting in an estimated bias of approximately 2 ms^{-1}.

Regarding vertical wind speed, lidar measurements indicate an average speed close to zero, which aligns with the EKF estimates. Among the configurations, EKF 3 shows a slightly lower average vertical wind speed.

Finally, a comparison with ground-level wind measurements reveals a substantial wind veer, which the EKF effectively
570 captures. Although the extrapolation of wind speed to the kite height provides velocities of a similar magnitude, these ground measurements cannot accurately capture wind speed variations at altitude.

Fig. 19 presents the 10-minute averaged wind speed and direction profiles for the same flight. The results show that incorporating the apparent wind speed yields the most accurate estimates of the wind speed profile. At the same time, all models provide similarly accurate estimates of wind direction, closely following the lidar measurements. The largest deviations from
575 the lidar data occur at altitudes above 200 m, corresponding to the reel-in phase. These discrepancies may be due to the degradation in the quality of position and velocity measurements, as discussed earlier.
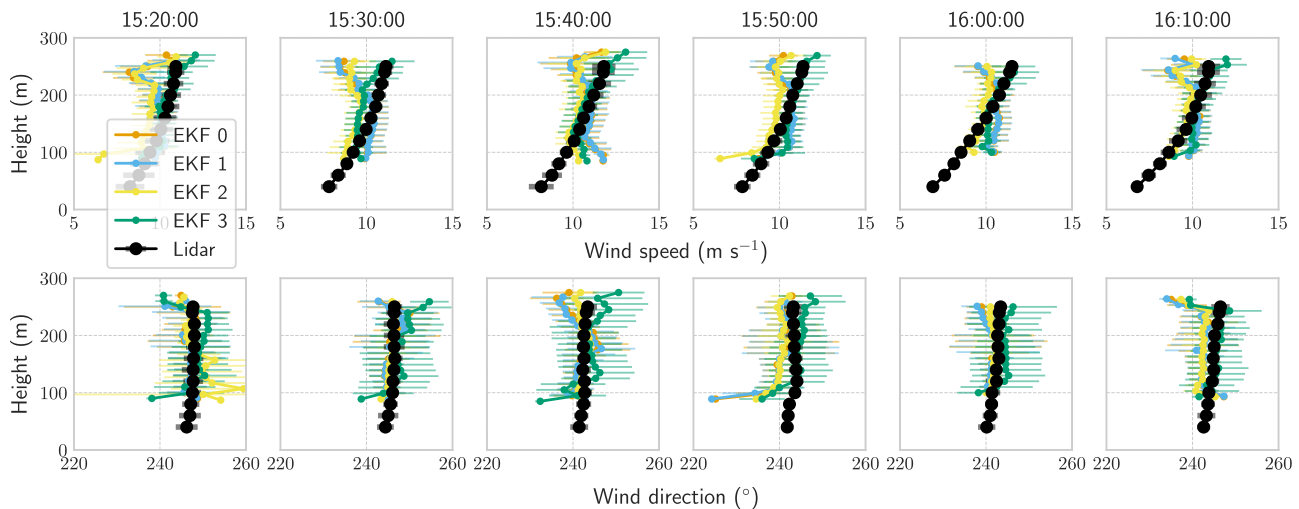
Figure 19. Test flight from 27-11-2023. Wind profile comparison between EKF model wind speed and direction estimates with a minimum sensor input setup, three variants with additional inputs, and lidar observations.

In contrast to the typical wind profile of the 2023-flight, the 2024-flight, shown in Fig. 20, featured a wind gust starting around 13:40, accompanied by a shift in wind direction that remained fairly constant until the gust subsided. During this flight, lidar data was available at a higher resolution of 1 second, with measurements presented at three different heights. Additionally,
580 measurements of the tether angles at the winch outlet were included in the model EKF 5. It is important to note that the IMU readings from the Pixhawk during this flight struggled to keep up with the high accelerations experienced during turns, resulting in clamped acceleration values and deteriorated measurements of the kite kinematics. This issue affected the performance of the EKF and led to non-physical peaks in the wind velocity estimates. Although adding additional measurements helped mitigate
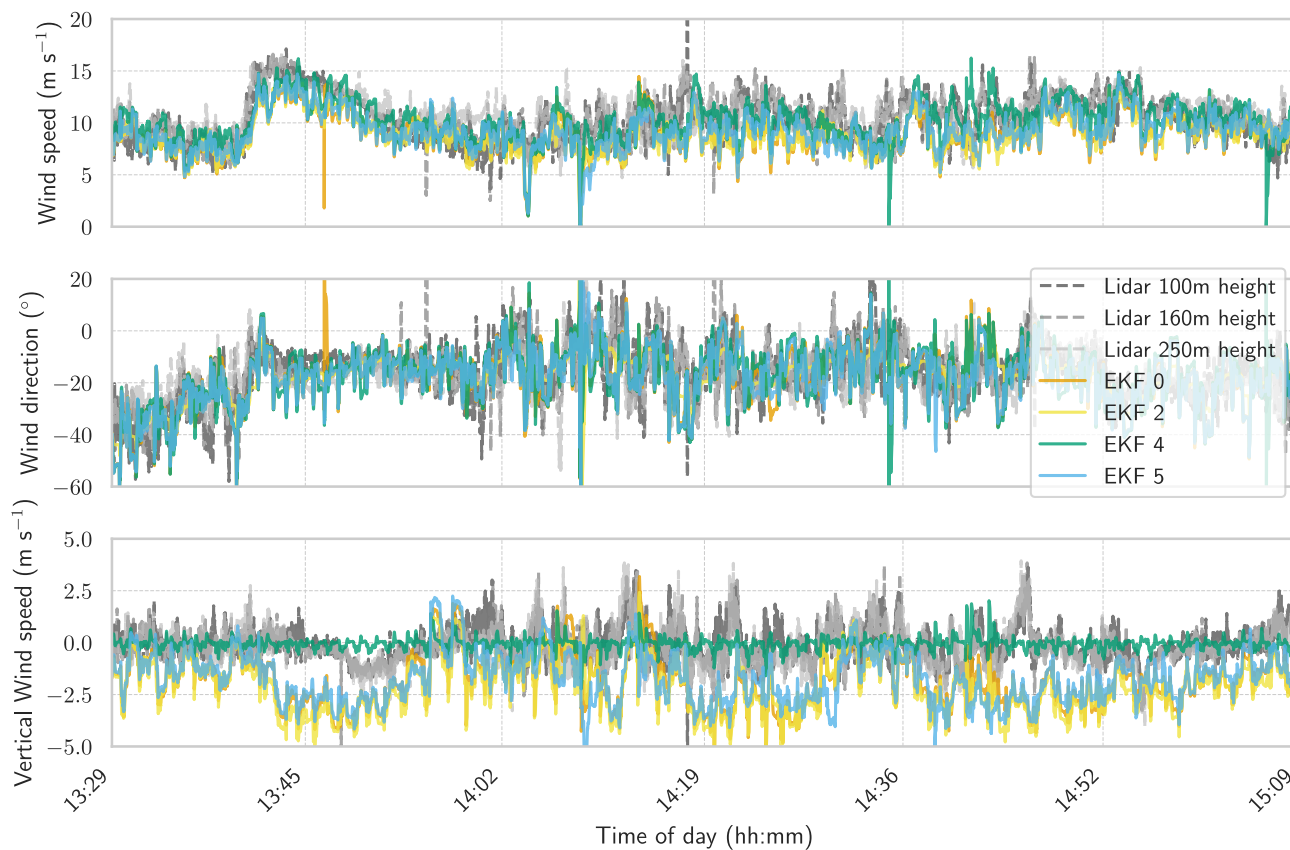
Figure 20. Test flight from 05-06-2024. Wind profile comparison between EKF results with a minimum sensor setup and lidar observations.

some of these peaks, such as the one observed at 13:47, it did not lead to significant improvements throughout the rest of the
585 flight.

A more detailed analysis of the shape of the wind profile during the wind gust event is shown in Fig. 21. By incorporating a zero vertical wind speed measurement (EKF 4), the time response of the wind model improves. In contrast, other models show a slower time response for horizontal wind speed and instead exhibit a decrease in vertical wind speed to match the same apparent wind speed. Furthermore, around 13:55, there is a localised increase in wind speed at higher altitudes that none of the
590 models can effectively capture. Apparent wind speed measurements might have been more effective at capturing these transient phenomena, but unfortunately, they were unavailable for this flight.

Regarding the wind direction, the time response appears to be better across all models, which similarly track the changes throughout the flight. The higher resolution of the lidar data also enables verification that the fluctuations in wind velocity align with the observations.
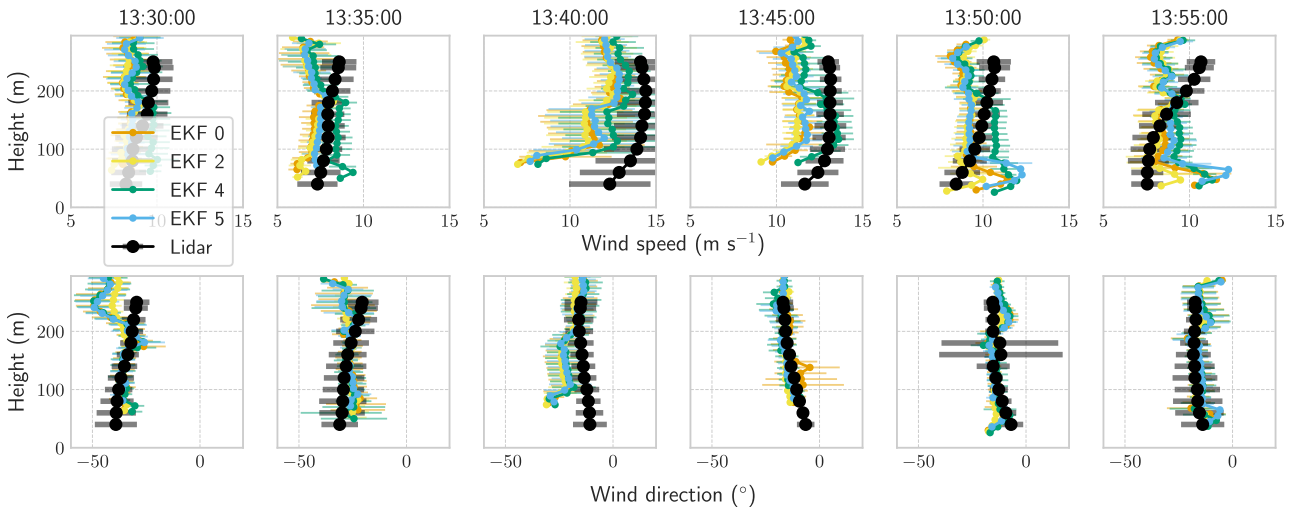
Figure 21. Test flight from 05-06-2024. Wind profile comparison between EKF results with a minimum sensor setup and lidar observations.

5.4 Turbulence measurements

Since the EKF estimates wind characteristics based on measurements that are not directly related to the inflow, accurate estimates of the variability in wind speed are highly dependent on the correct tuning of the filter. To verify that the rapid changes estimated are physical, one can examine the turbulence estimates, which quantify these variations.

A key aspect to investigate is the power density spectrum of the wind speed, as shown in Fig. 22. The sampling frequency of the measurements was $0.1\,\mathrm{s}$, corresponding to frequencies resolved of up to $5\,\mathrm{Hz}$. It is observed that the energy cascade follows the Kolmogorov slope within the range of $\sim 0.01\,\mathrm{Hz} - 0.3\,\mathrm{Hz}$, with higher frequencies damped, likely due to the time response of the EKF. Additionally, a peak is observed below $0.01\,\mathrm{Hz}$, corresponding to the cycle timescale for the analysed flight. This peak coincides with a rapid change in wind speed, attributed to the significant variation in kite height experienced during reel-in.

Another parameter assessed in the study is the turbulence intensity, defined as the standard deviation of the wind speed divided by its mean value. This parameter is commonly used in conventional wind energy assessments, particularly when assessing turbine fatigue loads. Turbulence intensity is also measured by the profiling lidar, providing an additional validation of the EKF. However, it is important to note that the quantities measured by the lidar and the EKF are not directly equivalent.

The lidar measures turbulence intensity over an averaged volume at a fixed height, with the area determined by the laser cone angle. In contrast, the turbulence intensity derived from the EKF is calculated over a range of heights within ±10m of the lidar measurement to obtain comparable values. It is calculated as the 1-minute standard deviation divided by the mean.

With these considerations in mind, we can compare the turbulence intensity estimates from both the EKF and lidar, as shown in Fig. 23 for the two analysed flights. The comparison reveals good agreement in magnitude, and the temporal behaviour of
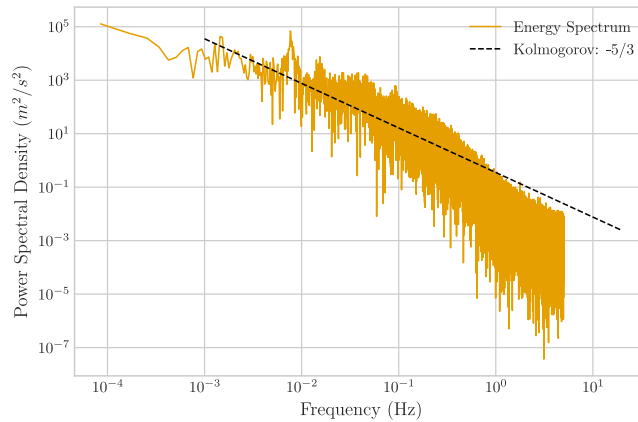
Figure 22. Test flight from 10-08-2019. Power spectral density of the wind speed.

the EKF closely matches that of the lidar, as illustrated in Fig. 23b. While these initial comparisons are promising, a more

615 detailed analysis is needed to fully assess the accuracy of these measurements.
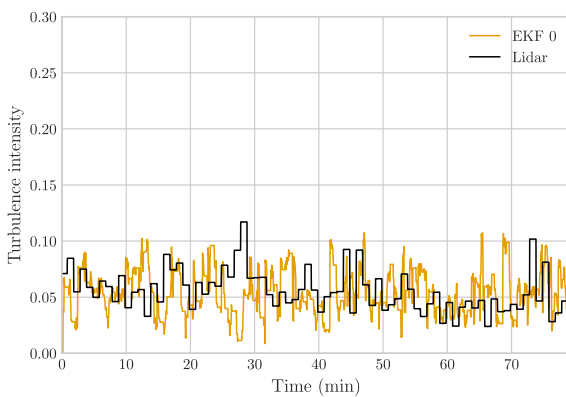
(a) V9 kite, flight 27-11-2023
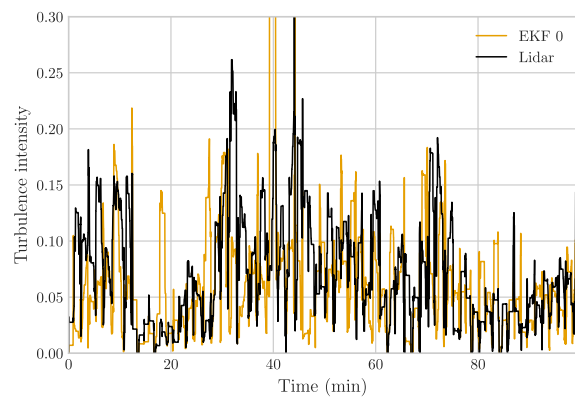
(b) V9 kite, flight 12-03-2024

Figure 23. Turbulence intensity at a height of 140m

6 Conclusions

This study presents a sensor fusion technique for tethered flying systems to estimate the state of the system and the wind conditions at the kite. The system state includes the kite's position, velocity, aerodynamic performance, and tether shape. The sensor fusion technique consists of an iterated extended Kalman filter (EKF), modelling the kite as a point mass and the tether

as a system of point masses linked by spring damper elements. The tether shape is assumed to be quasi-static and includes the robotic control unit as a point mass, linked to the kite by an additional spring damper element representing the bridle line system. By integrating data from multiple sensors, such as position, velocity, tether force, and reeling speed, the EKF model can accurately estimate system dynamics and wind conditions, provided the filter is appropriately tuned to the specific system configuration.

The proposed EKF effectively estimates average wind profiles, particularly those that follow a conventional logarithmic slope. However, its performance is less accurate in scenarios with significant deviations, such as sudden wind gusts, where the filter requires a few minutes to adapt to rapid changes in wind speed. Notably, the filter adapts faster to changes in wind direction, indicating greater sensitivity to directional variations. To improve the time resolution in wind estimations, direct airflow measurements should be included, such as a well-calibrated and maintained Pitot tube.

The accuracy of the estimations is highly dependent on the quality and reliability of the input measurements. While the EKF can compensate for minor inaccuracies and correct for biases in some measurements, substantial issues such as improperly calibrated sensors or malfunctioning equipment can significantly degrade the accuracy of wind speed and direction estimations.

Sensor noise and filter tuning are areas that deserve further attention. While the paper acknowledges the potential inaccuracies stemming from incorrect tuning and noise modelling, it does not discuss strategies to mitigate these problems in-depth. For the proposed EKF to be more robust for a specific system, it can be beneficial to incorporate a more comprehensive noise modelling. Implementing advanced calibration techniques, such as adaptive filtering methods for real-time sensor noise adjustments, could enhance the accuracy and reliability of state estimations.

The proposed approach also demonstrates the ability to estimate tether and kite orientations, which closely align with the measurements at the kite. This capability enables the estimation of the pitch deformations at the central struts of the wing relative to the tether, also referred to as the depower angle. This information can be used to estimate the wing angle of attack based on measurements made on the bridle lines. The kite was aerodynamically characterized for the range of flight conditions available using this newly estimated angle, showing an improvement with respect to previous analyses. However, for a complete aerodynamic characterization, tailored test flights must be conducted to capture the aerodynamic behaviour of the kite across different conditions.

This study explored several sensor setups, demonstrating that a single airborne sensor measuring the kite position and velocity, combined with ground-based force and tether length sensors, is sufficient to obtain reasonable estimates. While modelling the wind profile as logarithmic does not necessarily improve the estimates, it offers flexibility in independently tuning the process noise of wind speed and direction, which can be useful for supervisory control where high-frequency variations need damping. Adding a zero vertical wind speed measurement could improve the filter time response during transient events by preventing the misinterpretation of horizontal wind speed changes as vertical wind variations. Installing well-calibrated flow sensors on the kite is essential for high-resolution wind velocity estimates. Furthermore, a high-resolution angle-of-attack sensor is strongly recommended to accurately capture the wing angle of attack changes and enable accurate aerodynamic characterization of the kite.

Overall, the EKF has proven to be a robust method for wind and state estimation for AWESs, demonstrating sufficient
655 accuracy for mean wind speed and direction estimation for power generation cycles. However, its responsiveness to rapid
changes in wind conditions is limited by the quality and availability of sensor data. Future work should focus on optimising
sensor setups and conducting targeted system identification test flights to capture dynamic states beyond normal operational
limits, ensuring the kite can be characterized fully. Ultimately, this study highlights that the kite can be effectively used as a
sensor, providing valuable insights into system dynamics and wind conditions.

660 *Code and data availability.* The code can be found in the attached Github repository. It is currently private, but will be made public when
the paper is published. https://github.com/ocayon/EKF-AWE.

The datasets can be found on different data repositories: 1. Flight data 08-10-2019, Schelbergen et al. (2024). 2. Flight data 27-11-2023,
Cayon et al. (2024a). 3. Flight data 05-06-2024, Cayon et al. (2024b). The flights from 2023 and 2024 are under one year embargo and will
be public in November 2025.

665 **Appendix A: System Specifications and Tuning Parameters**

This appendix provides detailed information about the components of the Airborne Wind Energy System (AWES) and the
specific tuning parameters used for the Extended Kalman Filter (EKF) implementation.

A1   System Description

Kite Parameters

Table A1. Kite specifications

Parameter	Value	Unit
Model Name	V3	–
Mass	15	kg
Area	19.75	m^2
Span	10	m

670 **Bridle and KCU Parameters**
Tether Parameters

A2   Tuning Parameters for EKF

Measurement Standard Deviations

Table A2. Kite Control Unit (KCU) specifications

Parameter	Value	Unit
KCU Length	1	m
KCU Diameter	0.48	m
$C_{\perp,\mathrm{kcu}}$	0.69	–
$C_{\parallel,\mathrm{kcu}}$	0.83	–
Mass	27.6	kg
Distance KCU to Kite	11.5	m
Total Length of Bridle Lines	96	m
Diameter of Bridle Lines	0.0025	m

Table A3. Tether specifications

Parameter	Value	Unit
Material	Dyneema-SK78	–
Density (ρ_t)	970	$\mathrm{kg\,m^{-3}}$
Young's Modulus (E)	132	GPa
Diameter	0.01	m
$C_{\perp}$	1.1	–
$C_{\parallel}$	0.01	–
Number of Elements	10	–

Model Standard Deviations

675 *Author contributions.* Conceptualisation, O.C. and R.S.; methodology, O.C.; software, O.C.; investigation, O.C.; writing—original draft preparation, O.C.; writing—review and editing, R.S.; supervision, R.S.; funding acquisition, R.S. All authors have read and agreed to the published version of the manuscript.

Competing interests. At least one of the (co-)authors is a member of the editorial board of Wind Energy Science. R.S. is a co-founder of and advisor for the start-up company Kitepower B.V., which is commercially developing a 100 kW kite power system and provided their test
680 facilities and staff for performing the in situ measurements described in this article. Both authors were financially supported by the European Union's Meridional project, which also provided funding for Kitepower B.V.

Table A4. Measurement standard deviations used in the EKF

Parameter	Value	Unit
Position ($\mathbf{r}_k$)	5	m
Velocity ($\mathbf{v}_k$)	2	m s^{-1}
Tether Length (l)	0.5	m
Tether Elevation (β_0)	3	°
Tether Azimuth (ϕ_0)	3	°
Position tether model	1×10^{-5}	m
Zero Vertical Wind Speed ($v_{\mathrm{w}}^{\mathrm{z}} = 0$)	2	m s^{-1}
Apparent Airspeed (v_{a})	1	m s^{-1}
Bridle Angle of Attack (α_b)	4	°

Table A5. Model standard deviations used in the EKF

Parameter	Value	Unit
Position ($\mathbf{r}_k$)	2.5	m
Velocity ($\mathbf{v}_k$)	1	m s^{-1}
Wind Velocity ($\mathbf{v}_w$)	0.1	m s^{-1}
Wind Friction Velocity (u_*)	0.002	m s^{-1}
Wind Direction (ϕ_{w})	0.2	°
Vertical Wind Speed ($v_{\mathrm{w}}^{\mathrm{z}}$)	0.01	m s^{-1}
Lift Coefficient (C_L)	0.01	–
Drag Coefficient (C_D)	0.003	–
Side Force Coefficient (C_S)	0.01	–
Tether Elevation (β_0)	5	°
Tether Azimuth (ϕ_0)	5	°
Tether Length (l)	0.1	m

Acknowledgements. This work has been supported by the MERIDIONAL project, which receives funding from the European Union's Horizon Europe Programme under the grant agreement No. 101084216. We acknowledge the use of OpenAI's ChatGPT and Grammarly for assistance in refining the writing style of this manuscript.

685 **References**

Bar-Shalom, Y., Li, X., and Kirubarajan, T.: Estimation with Applications to Tracking and Navigation: Theory, Algorithms and Software, John Wiley & Sons Inc., https://doi.org/10.1002/0471221279.ch11, 2002.

Blevins, R. D.: Applied fluid dynamics handbook, Van Nostrand Reinhold Co., New York, NY, ISBN 978-0-442-21296-4, 1984.

Bootle, W. J.: Forces on an inclined circular cylinder in supercritical flow, AIAA Journal, 9, 514–516, https://doi.org/10.2514/3.6213, 1971.

690 Borobia, R., Sanchez-Arriaga, G., Serino, A., and Schmehl, R.: Flight-Path Reconstruction and Flight Test of Four-Line Power Kites, Journal of Guidance, Control, and Dynamics, 41, 2604–2614, https://doi.org/10.2514/1.G003581, 2018.

Borobia-Moreno, R., Ramiro-Rebollo, D., Schmehl, R., and Sánchez-Arriaga, G.: Identification of kite aerodynamic characteristics using the estimation before modeling technique, Wind Energy, 24, 596–608, https://doi.org/10.1002/we.2591, 2021.

Cayon, O., Gaunaa, M., and Schmehl, R.: Fast Aero-Structural Model of a Leading-Edge Inflatable Kite, Energies, 16, 3061,
695 https://doi.org/10.3390/en16073061, 2023.

Cayon, O., Schmehl, R., Luca, A., and Peschel, J.: Kitepower flight data acquired on 27 November 2023, https://doi.org/10.5281/zenodo.14237421, 2024a.

Cayon, O., Schmehl, R., Luca, A., and Peschel, J.: Kitepower flight data acquired on 5 June 2024, https://doi.org/10.5281/zenodo.14238586, 2024b.

700 Dunker, S.: Tether and Bridle Line Drag in Airborne Wind Energy Applications, in: Airborne Wind Energy: Advances in Technology Development and Research, edited by Schmehl, R., pp. 29–56, Springer, Singapore, ISBN 978-981-10-1947-0, https://doi.org/10.1007/978-981-10-1947-0_2, 2018.

Elfert, C., Göhlich, D., and Schmehl, R.: Measurement of the turning behaviour of tethered membrane wings using automated flight manoeuvres, Wind Energy Science, 9, 2261–2282, https://doi.org/10.5194/wes-9-2261-2024, 2024.

705 Erhard, M. and Strauch, H.: Control of Towing Kites for Seagoing Vessels, IEEE Transactions on Control Systems Technology, 21, https://doi.org/10.1109/TCST.2012.2221093, 2012.

Ezzeddine, W., Schutz, J., and Rezg, N.: Pitot sensor air flow measurement accuracy: Causal modelling and failure risk analysis, Flow Measurement and Instrumentation, 65, 7–15, https://doi.org/10.1016/j.flowmeasinst.2018.10.021, 2019.

Fagiano, L. and Novara, C.: Automatic crosswind flight of tethered wings for airborne wind energy: a direct data-driven approach, IFAC
710 Proceedings Volumes, 47, 4927–4932, https://doi.org/10.3182/20140824-6-ZA-1003.01896, 2014.

Fagiano, L., Huynh, K., Bamieh, B., and Khammash, M.: Sensor fusion for tethered wings in airborne wind energy, in: 2013 American Control Conference, pp. 2884–2889, https://doi.org/10.1109/ACC.2013.6580272, 2013.

Fagiano, L., Huynh, K., Bamieh, B., and Khammash, M.: On sensor fusion for airborne wind energy systems, IEEE Transactions on Control Systems Technology, 22, 930–943, https://doi.org/10.1109/TCST.2013.2269865, 2014.

715 Fechner, U.: A Methodology for the Design of Kite-Power Control Systems, Ph.D. dissertation, Delft University of Technology, https://doi.org/https://doi.org/10.4233/uuid:85efaf4c-9dce-4111-bc91-7171b9da4b77, 2016.

Freter, J. H., Seel, T., Elfert, C., and Göhlich, D.: Motion Estimation for Tethered Airfoils with Tether Sag, in: 2020 IEEE International Conference on Multisensor Fusion and Integration for Intelligent Systems (MFI), pp. 114–120, https://doi.org/10.1109/MFI49285.2020.9235235, 2020.

720 Gibbs, B. P.: Advanced kalman filtering, least-squares and modeling : a practical handbook, Wiley, Hoboken, N.J., https://doi.org/10.1002/9780470890042, 2011.

Hesse, H., Polzin, M., Wood, T. A., and Smith, R. S.: Visual Motion Tracking and Sensor Fusion for Kite Power Systems, in: Airborne Wind Energy, edited by Schmehl, R., pp. 413–438, Springer, Singapore, https://doi.org/10.1007/978-981-10-1947-0_17, 2018.

Hoerner, S. F.: Fluid-dynamic Drag: Practical Information on Aerodynamic Drag and Hydrodynamic Resistance, Hoerner Fluid Dynamics, 1965.

Hummel, J., Göhlich, D., and Schmehl, R.: Automatic Measurement and Characterization of the Dynamic Properties of Tethered Membrane Wings, Wind Energy Science Discussions, pp. 1–24, https://doi.org/10.5194/wes-2018-56, 2018.

Kitepower, B. V.: Kitepower - Airborne Wind Energy, https://thekitepower.com/, 2024.

Leuthold, R.: Multiple-Wake Vortex Lattice Method for Membrane-Wing Kites, Master's dissertation, Delft University of Technology, https://doi.org/10.13140/RG.2.2.30811.41765, 2015.

Meriam, J. L., Kraige, L. G., and Bolton, J. N.: Engineering Mechanics: Dynamics, John Wiley & Sons, 9th edn., ISBN 978-1-119-39098-5, 2018.

Oehler, J. and Schmehl, R.: Aerodynamic characterization of a soft kite by in situ flow measurement, Wind Energy Science, 4, 1–21, https://doi.org/10.5194/wes-4-1-2019, 2019.

Oehler, J., Marc, v. R., and Schmehl, R.: Experimental investigation of soft kite performance during turning maneuvers, Journal of Physics: Conference Series, 1037, 052 004, https://doi.org/10.1088/1742-6596/1037/5/052004, 2018.

Peschel, J.: A Cost-Effective Kite State Estimator for Reliable Automatic Control of Kites, Master's dissertation, TU Berlin, https://doi.org/10.5281/zenodo.7864661, 2013.

Poland, J. and Schmehl, R.: Modelling Aero-Structural Deformation of Flexible Membrane Kites, Energies, 16, 5264, https://doi.org/10.3390/en16145264, 2023.

Poland, J. and Schmehl, R.: TUDELFT_V3_LEI_KITE, https://github.com/awegroup/TUDELFT_V3_LEI_KITE, 2024.

Polzin, M., Wood, T. A., Hesse, H., and Smith, R. S.: State Estimation for Kite Power Systems with Delayed Sensor Measurements, IFAC-PapersOnLine, 50, 11 959–11 964, https://doi.org/10.1016/j.ifacol.2017.08.1176, 2017.

PX4: Using the ECL EKF | PX4 Guide, https://docs.px4.io/main/en/advanced_config/tuning_the_ecl_ekf.html, 2024.

Ranneberg, M.: Sensor Setups for State and Wind Estimation for Airborne Wind Energy Converters, CoRR, abs/1309.1029, http://arxiv.org/abs/1309.1029, arXiv: 1309.1029, 2013.

Roullier, A.: Experimental analysis of a kite system's dynamics, Master's dissertation, Delft University of Technology, https://doi.org/10.5281/zenodo.7752407, 2020.

Schelbergen, M.: Power to the airborne wind energy performance model, Ph.D. dissertation, Delft University of Technology, https://resolver.tudelft.nl/uuid:353d390a-9b79-44f1-9847-136a6b880e12, 2024.

Schelbergen, M. and Schmehl, R.: Swinging motion of a kite with suspended control unit flying turning manoeuvres, Wind Energy Science, 9, 1323–1344, https://doi.org/10.5194/wes-9-1323-2024, 2024.

Schelbergen, M., Schmehl, R., Buchholz, B., Breuer, J., and Peschel, J.: Kite power flight data acquired on 8 October 2019, https://doi.org/10.4121/19376174.V1, 4TU.Centre for Research Data [data set], 2024.

Schmidt, E., De Lellis, M., Saraiva, R., and Trofino, A.: State Estimation of a Tethered Airfoil for Monitoring, Control and Optimization, IFAC-PapersOnLine, 50, 13 246–13 251, https://doi.org/10.1016/j.ifacol.2017.08.1960, 2017.

Schmidt, E., Oliveira, M. D. L. C. D., Silva, R. S. D., Fagiano, L., and Neto, A. T.: In-Flight Estimation of the Aerodynamics of Tethered Wings for Airborne Wind Energy, IEEE Transactions on Control Systems Technology, 28, 1309–1322, https://doi.org/10.1109/TCST.2019.2907663, 2020.

760 Sommerfeld, M., Crawford, C., Monahan, A., and Bastigkeit, I.: LiDAR-based characterization of mid-altitude wind conditions for airborne wind energy systems, Wind Energy, 22, 1101–1120, https://doi.org/10.1002/we.2343, 2019.

Thedens, P. and Schmehl, R.: An Aero-Structural Model for Ram-Air Kite Simulations, Energies, 16, 2603, https://doi.org/10.3390/en16062603, 2023.

Vaisala: Wind Energy, WindCube, https://www.vaisala.com/en/products/wind-energy-windcube, 2020.

765 Viré, A., Lebesque, G., Folkersma, M., and Schmehl, R.: Effect of Chordwise Struts and Misaligned Flow on the Aerodynamic Performance of a Leading-Edge Inflatable Wing, Energies, 15, https://doi.org/10.3390/en15041450, 2022.

Vlugt, R. v. d., Peschel, J., and Schmehl, R.: Design and Experimental Characterization of a Pumping Kite Power System, in: Airborne Wind Energy, edited by Ahrens, U., Diehl, M., and Schmehl, R., pp. 403–425, Springer Berlin Heidelberg, Berlin, Heidelberg, https://doi.org/10.1007/978-3-642-39965-7_23, 2013.

770 Watson, S.: The Atmospheric Boundary Layer, in: Handbook of Wind Resource Assessment, pp. 11–32, John Wiley & Sons, Ltd, https://doi.org/https://doi.org/10.1002/9781119055402.ch2, 2023.

Williams, P.: Cable Modeling Approximations for Rapid Simulation, Journal of Guidance, Control, and Dynamics, 40, 1779–1788, https://doi.org/10.2514/1.G002354, 2017.

Williams, P., Lansdorp, B., and Ockels, W.: Nonlinear Control and Estimation of a Tethered Kite in Changing Wind Conditions, Journal of
775 Guidance Control and Dynamics, 31, https://doi.org/10.2514/1.31604, 2008.

Wood, T. A., Hesse, H., Polzin, M., Ahbe, E., and Smith, R. S.: Modeling, Identification, Estimation and Adaptation for the Control of Power-Generating Kites∗, IFAC-PapersOnLine, 51, 981–989, https://doi.org/10.1016/j.ifacol.2018.09.066, 2018.